Environmental Physics
University Bremen
Alfred-Wegener-Institut Bremerhaven

Master's Thesis

The Effect of Calendar Correction on North Atlantic Climate During the Last Interglacial

---

Mareike Mammes
Matriculation number: 6221648
E-Mail: mmammes@uni-bremen.de

Examiners: Prof. Dr. Gerrit Lohmann
PD Dr. Martin Werner

Advisor: Fernanda DI Alzira Oliveira Matos

Date of submission: 29 August 2025

Universität Bremen

ALFRED-WEGENER-INSTITUT
HELMHOLTZ-ZENTRUM FÜR POLAR- UND MEERESFORSCHUNG

Abstract

The Last Interglacial (LIG) is a period of great interest for paleoclimate studies, as temperatures were comparable to or slightly above today's. Orbital forcing led to Arctic Amplification, with strong warming in high latitudes of the Northern Hemisphere (NH) and a reduction in Arctic summer sea ice. The aim of this master's thesis is, firstly, to analyse the changes in seasonality during the LIG compared to the Pre-Industrial Period (PI). Secondly, it is investigated how applying a calendar based on astronomical positions instead of the modern Gregorian calendar impacts climate model results and where on Earth this effect is the greatest. The simulation runs for this thesis follow CMIP6 experiment protocols and were conducted using the climate model AWI-CM3.

It was found that an increase in incoming solar radiation during boreal summer leads to higher temperatures over the NH continents and over the Arctic region. The strongest warming occurs over North America and Eurasia and reaches more than +8 °C. During boreal summer and autumn, the Arctic sea ice concentration is lowered significantly. Changes in precipitation patterns lead to enhanced summer monsoons on the NH.

The differences between the angular calendar, based on astronomical positions, and the Gregorian calendar were found to be close in magnitude to the observed changes between LIG and PI for the atmosphere. The greatest differences between the two applied calendars occur in boreal autumn, and they are most pronounced in the mid- and high latitudes on the NH. For the surface ocean and Arctic sea ice, the deviations were smaller, but not negligible. Thus, a calendar correction should be applied for investigations of the LIG climate, especially when the North Atlantic and the Arctic region are evaluated.

Contents

List of Abbreviations

AWI-CM3 Third version of the Alfred Wegener Institute Climate Model utilised for the paleoclimate simulations for this thesis

BP Before present

CE Common Era

CMIP6 Sixth phase of the Coupled Model Intercomparison Project

DJF December, January, February; used synonymously to Northern Hemisphere winter

ECMWF European Centre for Medium-Range Weather Forecasts

FESOM2 Finite-volumE Sea ice–Ocean Model version 2

IPCC Intergovernmental Panel on Climate Change

GHG Greenhouse gas

ITCZ Intertropical Convergence Zone

JJA June, July, August

LIG Last Interglacial (129 000 – 116 000 years before present)

MAM March, April, May

MIS Marine Isotope Stage

NH Northern Hemisphere

PI Pre-Industrial Period (1850 CE)

PMIP4 Fourth phase of the Paleoclimate Modelling Intercomparison Project

psu Practical salinity unit; 1 psu is defined as 1 g of salt per 1000 g of water

SAT Surface air temperature

SH	Southern Hemisphere
SIC	Sea ice concentration
SON	September, October, November
SSS	Sea surface salinity
SST	Sea surface temperature
TOA	Top of the atmosphere

1 Introduction

Paleoclimate modelling is an important laboratory to investigate past climate, and to test climate models utilised for the representation of current climate and projection of future climate change (IPCC, 2021). As instrument-based observations of past climate are sparse in both spatial and temporal distribution, paleo records can be used to extend observations back in time in the form of reconstructions, providing a long-term context for recent and future climate changes (IPCC, 2021; Otto-Bliesner et al., 2021). For instance, paleoclimate data can be used to test climate models on climate states that differ from the climate documented in observations, to investigate multi-centennial and multi-millennial variability, and to constrain the equilibrium climate sensitivity (Kageyama et al., 2024). To assess the implications of greenhouse gas-driven climate change on the future climate, different geologic periods are suggested as potential analogues, e.g. the Early Eocene (ca. 50 million years (Ma) before present), the Mid-Pliocene (3.3 – 3.0 Ma) or the Last Interglacial (see below; Burke et al., 2018).

The current geologic period, the Quaternary (2.58 million years ago to present), is mainly characterised by glacial-interglacial cycles that modify Earth's climate at relatively short timescales through the recurrent build-up and melting of ice sheets. Glacials are periods when temperatures are relatively colder and glaciers advance, whereas interglacials are marked by comparably warmer temperatures and retreating glaciers (Grotzinger and Jordan, 2017). The current interglacial, the Holocene, started around 11,700 years before present (BP) and was preceded by the Last Interglacial (LIG; 129 000 – 116 000 years BP), which is deemed as the last period when the global mean temperature was comparable to or warmer than today (Kukla et al., 2002).

The exact extent of warming during the LIG is still debated, the latest report of the Intergovernmental Panel on Climate Change (IPCC) states a warming in the range of (0.5 to 1.5) °C (IPCC, 2021). Changes in orbital forcing (see Section 2.1 "Orbital parameters that affect Earth's climate") led to Arctic Amplification, causing very warm summers in the high latitudes on the Northern Hemisphere. For

this reason, the LIG is often seen as an analogue to anthropogenic climate change, associated with Arctic Amplification and a decline in Arctic sea ice, even though the forcings differ (Yin and Berger, 2015; Sicard et al., 2023). While current climate change is driven by greenhouse gas emissions (IPCC, 2021), the driver of LIG climate were variations in orbital forcing.

During the LIG, the eccentricity was larger than during the PI and Earth was at perihelion close to boreal summer solstice (e.g. Otto-Bliesner et al., 2017). Because of that, the lengths of seasons vary significantly between LIG and PI (Joussaume and Braconnot, 1997). If not taken into account, the difference in the length of seasons can have an impact on the paleoclimate model output that can easily be misinterpreted (see Section 2.3 "Paleo calendar effect"). Even though it was found in Joussaume and Braconnot (1997) that this effect may introduce a large bias in the analysis of the data, it is still often not considered in paleoclimate modelling (Bartlein and Shafer, 2019).

The aim of this thesis is therefore to investigate the changes in climate during the LIG relative to the PI and how they are impacted by the chosen calendar. Special focus will be laid on determining when and in which regions the paleo calendar effect is most pronounced and which processes are most affected.

2 Background

In the 19th century, Earth scientists discovered that large parts of Europe and North America had been covered by glaciers in the past and began to debate the cause of a colder climate allowing ice sheets to persist (Raymo and Huybers, 2008). Still favoured today is the theory by Serbian scientist Milutin Milankovitch, often called the Milankovitch theory. It states that the incoming solar radiation (insolation) received by the Northern Hemisphere (NH) in summer is critical for the accumulation or ablation of ice sheets (Milanković, 1941). The NH summer insolation varies over time, driven by changes in Earth's orbit around the Sun, and in this way acts as the driver of glacial-interglacial cycles (Hays et al., 1976).

In the following section, more in-depth descriptions will be given of the orbital parameters that affect climate on Earth, the climate during the LIG, the paleo calendar effect, and a method to circumvent this issue, the calendar correction.

2.1 Orbital parameters that affect Earth's climate

Variations in Earth's orbit around the Sun can be described by the three orbital parameters: obliquity (obl), eccentricity (e) and precession (ω). On a timescale of ten thousands to hundred thousands of years, they lead to changes in the seasonal and latitudinal distribution of insolation and act as a pacemaker for glacial-interglacial cycles (Hays et al., 1976; Berger, 1988). The orbitally driven changes in insolation reaching the top of the atmosphere have been calculated in the past by Berger and Loutre (1991) and by Laskar et al. (1993); Laskar et al. (2004).

Obliquity. The obliquity, also called the axial tilt, describes the angle between the rotational axis of Earth and the orbital plane on which Earth revolves around the Sun. It varies between 22.05° and 24.5°, with a period of 41 000 years.
Obliquity is the main driver of seasonal variations in insolation. During NH summer, the NH is tilted towards the Sun, receiving more incoming solar radiation in consequence. Meanwhile, the Southern Hemisphere (SH) is tilted away from the Sun, receiving less insolation. A stronger tilt leads to enhanced seasonality, especially at

high latitudes (Cronin, 2010).

Eccentricity. The eccentricity is a measure of the orbit's deviation from a circle. In the past, it varied between 0.005 and 0.0607, where an eccentricity of exactly zero would describe a perfect circle. These variations happen on two main periods of approximately 413 000 years and 100 000 years (Ruddiman, 2014). The eccentricity leads to a difference in insolation between perihelion, the closest point to Sun along the orbit, and aphelion, where Earth is the farthest from Sun. However, the effect of eccentricity variations on the global mean insolation is relatively small (Cronin, 2010). It can however lead to a modulation and amplification of the obliquity and precession signals through internal feedbacks (Imbrie et al., 1993; Cronin, 2010).

Precession. The positions of the solstices and equinoxes slowly shift over time with respect to the positions of perihelion and aphelion. This is caused by the precession, which consists of two components: the axial and the elliptical precession.

The axial precession is a result of the torque of the Sun and the Moon on the bulge in Earth's diameter at the Equator. It leads to a wobbling motion, causing Earth's rotational axis to prescribe a circle over a period of 25 700 years. The elliptical precession is a rotation of the elliptical orbit on which Earth revolves around the Sun. The cause of this are planetary effects on Earth's mass. In combination, the precession leads to the equinoxes and solstices moving around Earth's orbit with a period of approximately 22,000 years. This results in a varying distance of the equinox and solstice positions from the Sun. Currently, the 21 June solstice occurs close to the aphelion. As a consequence, less insolation reaches the top of the atmosphere (TOA) in NH summer (SH winter). At the 21 December solstice, Earth is close to perihelion and receives slightly more incoming solar radiation. The eccentricity has an impact on the amplitude of these changes: at times of greater eccentricity, the difference in distance from Earth to Sun between perihelion and aphelion is enhanced. Consequently, the insolation changes are also amplified in comparison to a more circular orbit. Therefore, the precession is often expressed in terms of the precessional index, $e \sin \omega$, where e is the eccentricity and $\sin \omega$ is the sine wave representation of the movements of the equinoxes and solstices (Cronin,

2010; Ruddiman, 2014).

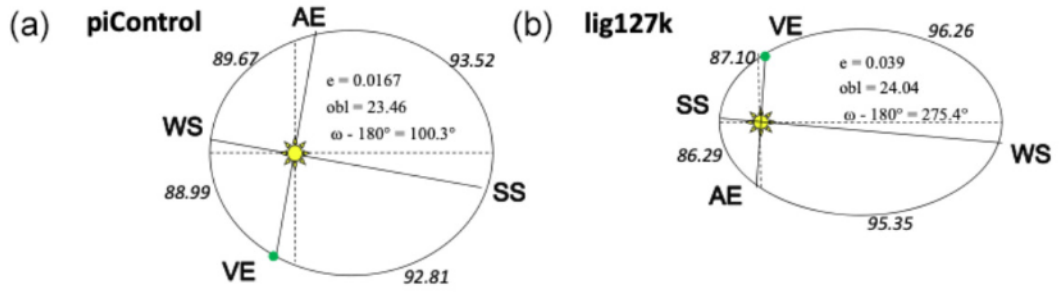

Figure 2.1: Orbital configurations for (a) 1850 CE and (b) 127 000 (BP) as described in the experimental protocols for *piControl* and *lig127k* (reprinted from Otto-Bliesner et al., 2021). Values for eccentricity, obliquity and precession are denoted inside the ellipse, days between equinoxes and solstices along the outside of the ellipse.

During the LIG, the orbital parameters differed significantly from those in the PI. Figure 2.1 shows a sketch of the orbital configurations during LIG and PI as used for the PMIP4 experiments. In comparison to the PI, the orbit was more elliptical and perihelion occurred close to summer solstice, instead of winter solstice, during the LIG. This leads to the seasonality being enhanced on the NH, and attenuated on the SH.

Furthermore, in accordance with Kepler's second law, Earth moves faster close to perihelion and slower close to aphelion, reducing the duration of NH summer (SH winter) and extending NH winter (SH summer). The increased obliquity enhances the seasonal differences on both hemispheres, especially for high latitudes.

2.2 The climate during the Last Interglacial

The Last Interglacial started around 129 000 years BP and ended at around 116 000 years BP with the onset of the last glaciation, and was the last period when temperatures were comparable to or even warmer than today (Kukla et al., 2002). It corresponds to Marine Isotope Stage 5e (MIS 5e), and is also referred to as the Eemian in northern Europe. As it is the most recent interglacial before the Holocene, there are more proxy data available than for the interglacials preceding the LIG

(Otto-Bliesner et al., 2013; Bakker et al., 2013). Still, there are quite a few uncertainties about the climate during the LIG. For instance, the global mean temperature is still a matter of debate.

Turney and Jones (2010) report a warming of $(1.5 \pm 0.1)\,°C$ relative to the 1961–1990 average for the global mean surface air temperature based on a paleoclimate reconstruction consisting of ice, marine and terrestrial data. The multi model mean of the model ensemble used in the sixth phase of the Coupled Model Intercomparison Project (CMIP6) amounted to a temperature change of $(-0.20 \pm 0.32)\,°C$ compared to the Pre-Industrial Period (PI; 1850 CE (Common Era)), with models ranging from $(-0.48$ to $0.56)\,°C$ (Otto-Bliesner et al., 2021). Scussolini et al. (2019) analysed the agreement between models and reconstructions for precipitation during the LIG. They found that models and reconstructions agree on an increased precipitation in boreal summer on the NH, but show disagreement over the SH.

Changes in orbital forcing led to Arctic Amplification associated with considerably higher temperatures over high latitude continents. Dahl-Jensen et al. (2013) report a peak warming of $(8 \pm 4)\,°C$ at the drilling site of the NEEM ice core in Greenland, while CAPE (2006) estimate a warming of $4\,°C$ to $5\,°C$ over Arctic lands during summer.

Arctic summer sea ice is also still strongly debated. While some studies indicate perennial sea ice in the Arctic (Stein et al., 2017; Kremer et al., 2018), others suggest a seasonally ice-free Arctic (Sime et al., 2023; Vermassen et al., 2023). The global mean sea level was 6 to 9 m higher than present due to thermal expansion as well as mass loss from the Greenland and Antarctic ice sheets (Dutton et al., 2015).

2.3 Paleo calendar effect

There are two ways to define months or seasons that are often used in paleoclimate modelling (Joussaume and Braconnot, 1997; Bartlein and Shafer, 2019):

1. the classical or "fixed-length" definition: a month (or season) is defined by a fixed number of days (typically according to the modern Gregorian calendar)

2. the angular or "fixed-angular" definition: a month (or season) is defined by

the time it takes Earth to traverse a fixed number of degrees along Earth's orbit around the Sun (e.g. 30° per month or 90° per season)

The term "paleo calendar effect" describes the impact that changes in the length of seasons over the geological timescale have on the analysis of climate model output (Bartlein and Shafer, 2019). These variations in the length of seasons are caused by the fluctuations in precession and eccentricity. According to Kepler's second law, months and seasons are shorter when Earth is close to perihelion and longer when close to aphelion. A larger eccentricity enhances this effect. Another consequence of orbital variations, more precisely of the precession, is that the time when Earth reaches perihelion is shifted. Thus, when the same date in two different paleoclimatic periods is compared while applying the modern calendar, it can lead to a comparison of two completely different positions along Earth's orbit (Kutzbach and Gallimore, 1988; Joussaume and Braconnot, 1997). The paleo calendar effect can result in patterns in the model output that can be misinterpreted as climatic changes, primarily emerging when model output is averaged over months or seasons, but can even slightly impact annual means (Bartlein and Shafer, 2019). Examples of misinterpreted climate change include amplified or dampened temperature changes, contrasts between the hemispheres, variations in the monsoonal strength, and a latitudinal shift of monsoon regions and the Intertropical Convergence Zone (ITCZ).

For the LIG, several studies indicate a relatively significant change in the length of seasons under the angular calendar, relatively to the classical calendar, particularly during NH autumn. The sensitivity of paleoclimate simulations to changes in seasonality during the LIG was examined in Joussaume and Braconnot (1997) with the conclusion that the paleo calendar effect is in the same order of magnitude as the Milankovitch forcing. Therefore, a calendar correction is strongly advisable for investigations of the climate during the LIG.

2.4 Calendar correction

For the conversion of the Gregorian calendar to an angular calendar, the time that has elapsed since perihelion was passed needs to be calculated. This problem is

described in detail e.g. in Chapter 3 of Curtis (2014) and defined in the following equations.

To relate the position along the orbit to the elapsed time, we define the angle between perihelion and the position as the true anomaly θ. As a first step, the mean anomaly, M, defined as the angle between perihelion and Earth's position if Earth moved with constant velocity along a circular orbit for the same period of time, is calculated:

$$M = \frac{2\pi}{T} \cdot t_p, \tag{2.1}$$

where t_p represents the time elapsed since perihelion was passed, and T the orbital period (1 year).

As Earth's orbit around the Sun is in fact not circular but elliptical, M in Equation 2.1 is modified:

$$E - \epsilon \cdot sin(E) = M, \tag{2.2}$$

where E is the eccentric anomaly, and ϵ is the eccentricity. Equation 2.2 is called Kepler's equation. It is a transcendental equation and must be solved iteratively, for example by using Newton's method (Curtis, 2014).

As we are interested in the true anomaly, θ, Equation 2.1 shows that:

$$t_p(\theta) = \frac{MT}{2\pi}. \tag{2.3}$$

Substituting M from Equation 2.5 into Equation 2.4 yields:

$$t_p(\theta) = \frac{(E - \epsilon \cdot sin(E))T}{2\pi}, \tag{2.4}$$

Equation 2.5 shows the relation between the eccentric anomaly E and the true anomaly θ (Eq. 3.13(b) in Curtis, 2014):

$$E = 2 \cdot arctan\left(\sqrt{\frac{1-\epsilon}{1+\epsilon}} \cdot tan\left(\frac{\theta}{2}\right)\right) \tag{2.5}$$

With the equations above, we can finally express the relation between the elapsed

time since perihelion t_p and the true anomaly θ as follows (Eq. 2.6):

$$t_p(\theta) = \frac{MT}{2\pi} = \frac{(E - \epsilon \cdot sin(E))T}{2\pi} \tag{2.6}$$

Although these sets of equations describe a relatively simple method, applying the calendar corrections is not a trivial process for modelling studies. In principal, as paleoclimate simulations require long integrations to reach a quasi-equilibrated state, they are often designed to store monthly output. Since the calendar correction is essentially a method that modifies the duration of months, the recommended output for application is of daily frequency. If only monthly data is archived, it needs to be interpolated to daily time steps first (Bartlein and Shafer, 2019), which can lead to spurious results. Interpolation methods that preserve monthly means are described in Epstein (1991) and Pollard and Reusch (2002). In this study, this issue was addressed by performing a quasi-equilibrated simulation with monthly output and branching off from this to simulate another 40 years with daily output.

3 Methods

The paleoclimate simulations featured in this thesis were conducted using the newly developed Alfred Wegener Institute Climate Model version 3.2 (AWI-CM3 hereafter). The model, the boundary conditions of the experiments, as well as the application of the calendar correction will be described in the following.

3.1 AWI-CM3 climate model

AWI-CM3 is an atmosphere-ocean general circulation model (AOGCM). A detailed description of the model and an evaluation of its performance can be found in Streffing et al. (2022). AWI-CM3 comprises of the ocean model FESOM2.5 (Finite-volumE Sea ice–Ocean Model; Danilov et al., 2017; Scholz et al., 2019, 2022) and the atmosphere component OpenIFS version 43r3, which is the open source version of the Integrated Forecast System (IFS) by the European Centre for Medium-Range Weather Forecasts (ECMWF; ECMWF, 2017a,b,c). Both components are coupled by the OASIS3-MCT4 coupler (Craig et al., 2017). Figure 3.1 schematically shows the components of AWI-CM3.

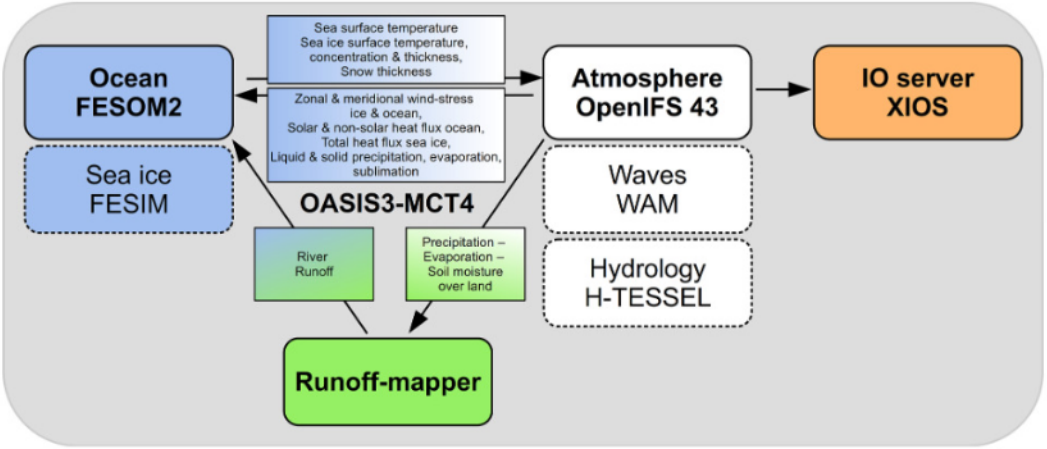

Figure 3.1: Schematic of the interactions between the different components in the coupled climate model AWI-CM3 (reprinted from Streffing et al., 2022).

FESOM2.5 (FESOM2 hereafter) is a global unstructured ocean model developed by the Alfred Wegener Institute. Its unstructured, triangular mesh allows for pro-

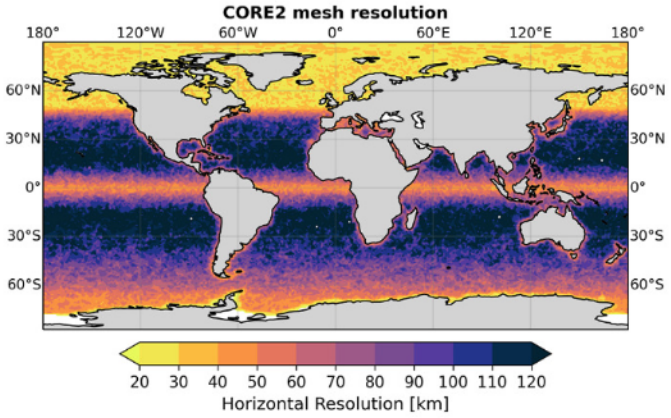

Figure 3.2: Horizontal resolution of the COREII mesh utilised by the ocean model FESOM2 for the simulations featured in this thesis (reprinted from Streffing et al., 2022).

cesses happening on smaller spatial scales to be resolved in relevant areas, e.g. near coastlines, in high latitudes and around the Equator. Compared to its predecessor, the computational efficiency was improved in the second version by the utilisation of a finite volume dynamical core as opposed to the previously used finite elements. Further, arbitrary Lagrangian Eulerian (ALE) vertical coordinates were introduced in the second version (Scholz et al., 2019). FESOM2 includes the sea ice model FESIM (Danilov et al., 2015). For the simulations here, the FESOM2 mesh prepared for the Coordinated Ocean-ice Reference Experiments (COREII; Large and Yeager, 2009) with approximately 127,000 surface nodes and 47 vertical levels was utilised. Its horizontal resolution ranges between 25 and 125 km depending on latitude and distance from the coast (see Figure 3.2, Streffing et al., 2022).

OpenIFS uses a semi-Lagrangian semi-implicit advection scheme which allows the simulations to be numerically stable at longer time steps than Eulerian schemes at similar resolutions (ECMWF, 2017a; Streffing et al., 2022). Its dynamical core and parameterisations, as well as its hydrology model H-TESSEL (Balsamo et al., 2009) and wave model WAM (Komen et al., 1994), are the same as used in the IFS suite. OpenIFS can be used in a wide range of horizontal resolutions. For this thesis, a cubic octahedral grid with spectral truncation at wavenumber 95 and with 91 vertical layers levels (TCo95L91) was applied, with a horizontal resolution of

approximately 100 km.

Auxiliary components handle the coupling of atmosphere and ocean, the routing of river runoff and the output of OpenIFS. The runoff mapper obtains the difference in precipitation, evaporation and soil moisture from OpenIFS and reroutes the excess water to the ocean via river basins (Streffing et al., 2022). The parallel XML I/O server XIOS replaces the sequential I/O scheme that is otherwise used for OpenIFS 43r3. This leads to a reduction in computational cost and an increase in integration speed, and furthermore allows for model output in NetCDF files instead of GRIB files (Streffing et al., 2022). To facilitate model compilation, as well as configuration and execution of the simulations, the ESM-Tools software package (Barbi et al., 2021) was utilised. For preprocessing of the model output, the Climate Data Operators toolset (CDO; Schulzweida, 2023) was applied.

Model evaluation

To evaluate how well the results of AWI-CM3 for the LIG match those of other simulations, a comparison with the model ensemble of the fourth phase of the Paleoclimate Modelling Intercomparison Project (PMIP4) will follow. For this purpose, the differences in surface air temperature and precipitation between LIG and PI are shown in Figures 3.3 and 3.4, respectively. For both the surface air temperature and the precipitation, the results utilising AWI-CM3 look similar to the PMIP4 multi-model means. A few differences are discernible, however. First, the results for the surface air temperature anomalies will be compared.

For the months December, January and February (DJF), the PMIP4 ensemble shows more warming over the Arctic region, while around the mid-latitudes, the continents on the NH exhibit slightly colder temperatures. Further, the tropical oceans and the SH continents appear a bit colder than simulated by AWI-CM3, especially the Antarctic. In June, July and August (JJA), AWI-CM3 results show more warming over the Southern Ocean, and again less warming over the Arctic region. For the annual mean surface air temperature anomalies, AWI-CM3 simulates colder temperatures in the North Pacific, around the Bering Strait, but less cooling

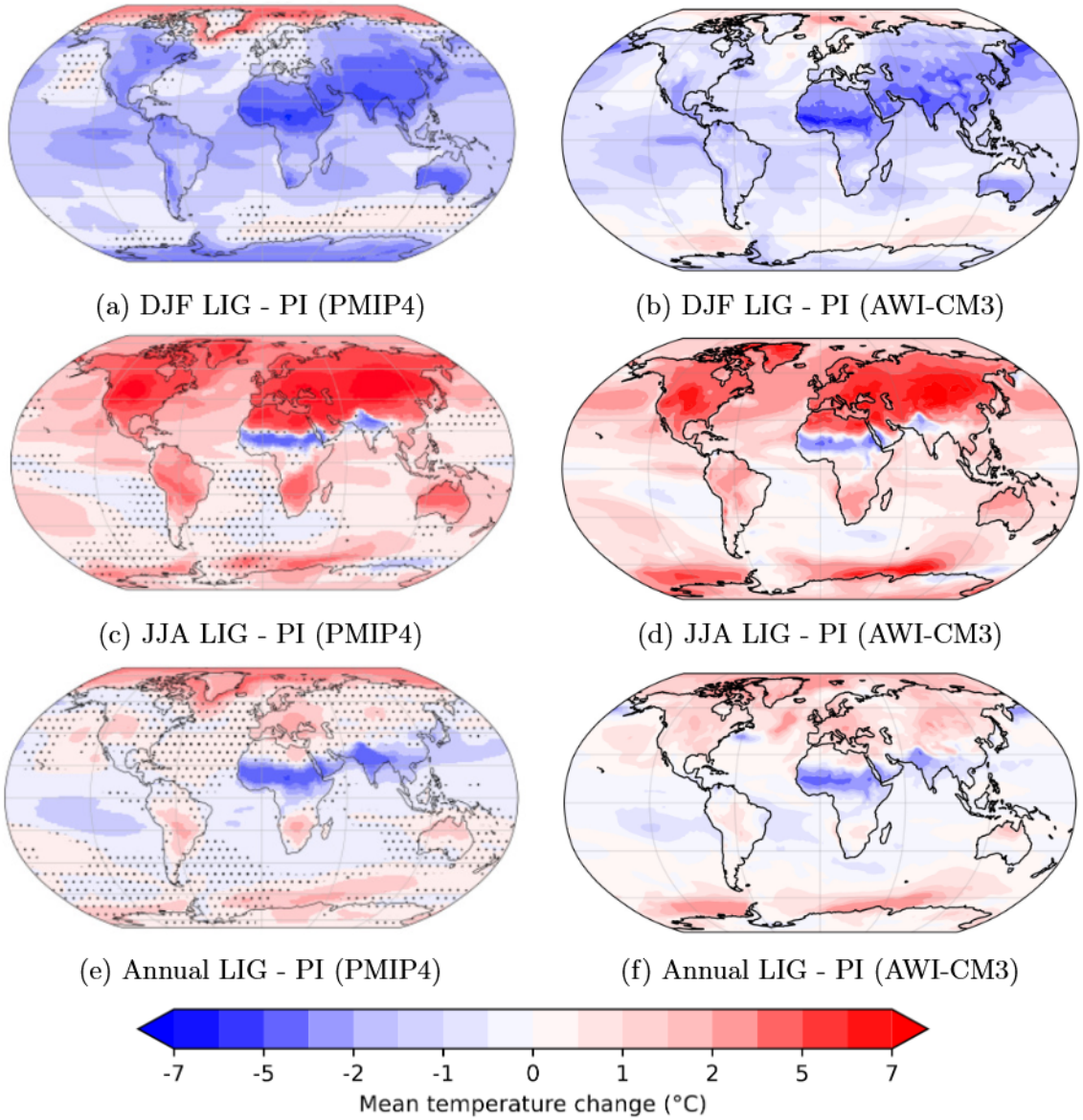

(a) DJF LIG - PI (PMIP4)

(b) DJF LIG - PI (AWI-CM3)

(c) JJA LIG - PI (PMIP4)

(d) JJA LIG - PI (AWI-CM3)

(e) Annual LIG - PI (PMIP4)

(f) Annual LIG - PI (AWI-CM3)

Figure 3.3: Seasonal and annual mean surface air temperature. (a), (c) and (e): Multi-model mean of the PMIP4 ensemble (adapted from Otto-Bliesner et al., 2021), (b), (d) and (f): AWI-CM3 results (using the angular calendar). In the plots of the PMIP4 model ensemble, dots indicate areas where less than 70 % of the 17 models agree on the sign of the change.

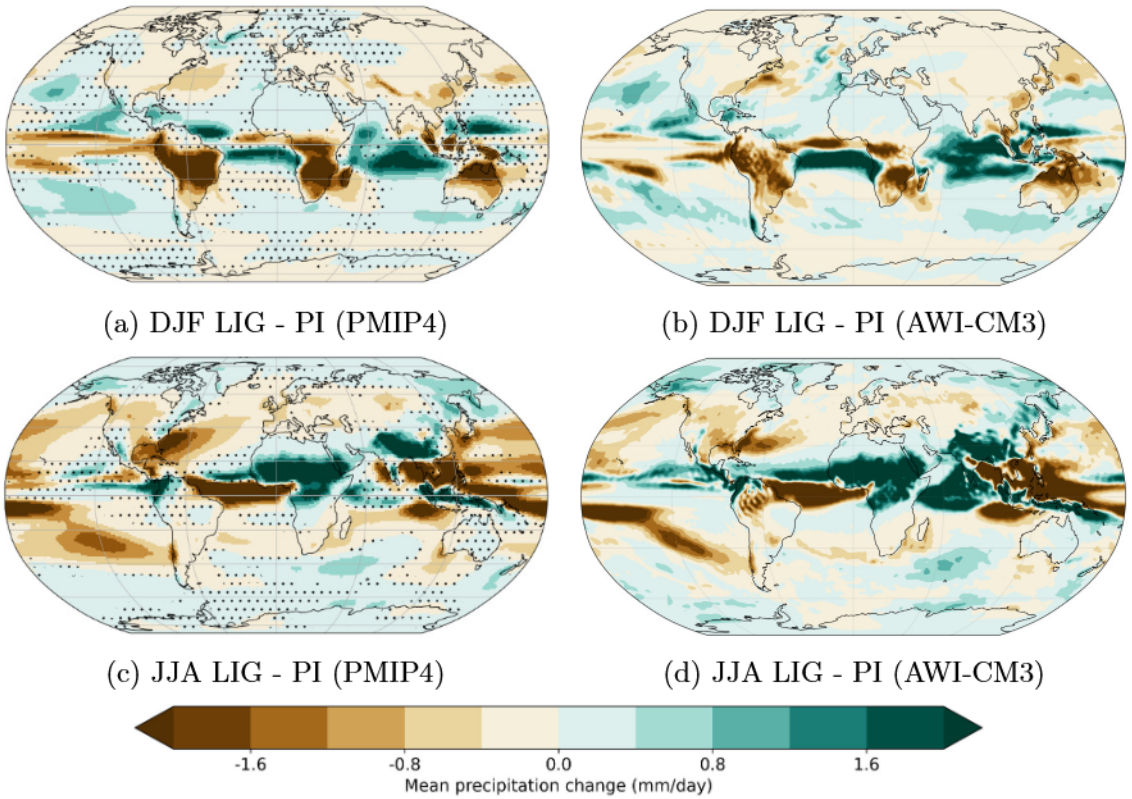

Figure 3.4: Seasonal mean precipitation. (a) and (c): Multi-model mean of the PMIP4 ensemble (adapted from Otto-Bliesner et al. (2021)), (b) and (d): AWI-CM3 results (using the angular calendar). In the plots of the PMIP4 model ensemble, dots indicate areas where less than 70 % of the 17 models agree on the sign of the change.

in the mid-latitudinal and subtropical Pacific. Like before, the Arctic region is slightly colder than shown by the PMIP4 models, especially around Greenland's coasts.

Differences between AWI-CM3 and PMIP4 results for the precipitation anomalies between LIG and PI mostly occur around the tropical rain belt. In DJF, the results of AWI-CM3 simulations show less drying over the equatorial Pacific and Atlantic, and also over the SH continents. More precipitation is observed over the Atlantic south of the Equator. In JJA, precipitation over the Indian Ocean is pronounced. Over the Pacific, drying is less extensive compared to the PMIP4 ensemble.

Overall, the results of AWI-CM3 and the PMIP4 ensemble show a good agreement for the surface air temperature and precipitation anomalies, but some differences occur, predominantly over the polar regions for temperature and over the

tropical rain belt for precipitation anomalies.

3.2 Experimental setup

For this thesis, two experiments were performed to simulate the climate during the LIG as well as the climate during the PI, which is used as a reference period. Each model run was designed to produce daily output over a period of 40 years. The two performed simulations differ in the orbital configuration and also in the prescribed greenhouse gas concentrations in the atmosphere. The continental configurations were left unchanged. The PI simulation was branched off from an existing spinup spanning 700 years, while the LIG simulation was branched off from an existing simulation of 1000 years. This was done to ensure that the results displayed here refer to quasi-equilibrated climate states and to enable comparison with the monthly output of the original simulations.

Pre-Industrial (*piControl*). The simulation of the PI follows the protocol of the *piControl* experiment that is part of the sixth phase of the Coupled Model Intercomparison Project (CMIP6). The aim of CMIP6 is to contribute to a better understanding of past, present and future climate change driven by natural variability or by changes in radiative forcing. By providing protocols with fixed boundary conditions for the different experiments and by standardising model output, the project ensures that the results of the participating models are comparable (Eyring et al., 2016).

A detailed description of the *piControl* experiment can be found in Eyring et al. (2016). It represents a period before the commence of large-scale industrialisation, with 1850 CE acting as reference year. The concentrations of atmospheric greenhouse gases (GHGs), land use, and orbital configurations are held fixed (see Table 3.1). This way, the internal variability of the climate system without anthropogenic forcing can be analysed. The solar forcing is set to the 1850 to 1873 mean of the CMIP6 historical simulation, volcanic aerosols are set to match the forcing during the historical simulation as closely as possible. Ice sheets and paleogeography are kept at modern values.

Last Interglacial (*lig127k*). The setup of the LIG experiment follows the PMIP4 protocol for the *lig127k* experiment described in Otto-Bliesner et al. (2017). It is one of two core interglacial experiments that are part of the fourth phase of the Paleoclimate Modelling Intercomparison Project (PMIP4). The aim of the interglacial experiments is to investigate the impact of orbital forcing on the climate system at times when boundary conditions (e.g. the continental margins) and other initial conditions (e.g. GHG concentrations) were similar to today. The reference year for the *lig127k* experiment is 127,000 years BP, which represents the early, warmest phase of the LIG. Orbital parameters follow Berger and Loutre (1991). Table 3.1 shows the prescribed values for the orbital parameters, the atmospheric GHG concentrations and other boundary conditions used for the two experiments.

Table 3.1: Experimental design implemented in the simulations featured in this thesis.

	piControl	*lig127k*
Orbital parameters		
Eccentricity	0.016 764	0.039 378
Obliquity (in degrees)	23.459	24.040
Perihelion - 180	100.33	275.41
Vernal equinox	21 March noon	21 March noon
Greenhouse gases		
Carbon dioxide (in ppm)	284.3	275
Methane (in ppb)	808.2	685
Nitrous oxide (in ppb)	273.0	255
Other GHGs	CMIP6 *piControl*	0
Solar constant (in W/m^2)	1360.747	Same as *piControl*
Paleogeography	Modern	Same as *piControl*
Ice sheets	Modern	Same as *piControl*
Vegetation	CMIP6 *piControl*	Prescribed or interactive as in *piControl*
Aerosols	CMIP6 *piControl*	Prescribed or interactive as in *piControl*

3.3 Calendar correction algorithm

The climate model AWI-CM3 applies the modern Gregorian calendar. As discussed before, for the LIG the paleocalendar effect can lead to a significant bias.

Therefore, the model output was converted to a fixed-length calendar using the algorithm described in Shi et al. (2022) (Python code and description available at `https://gitlab.awi.de/xshi/calendar`). For daily model output, the routines `calendar.py` and `newmonthlymeans_daily.py` can be used to calculate the days per month based on the orbital parameters and to determine monthly means from this, respectively.

The first step of the calendar correction is to set a starting point that will act as reference point to calculate the true anomaly. This will be the NH vernal equinox, set to 21 March at noon. In the following, the meteorological definition of seasons will be applied, meaning spring for example spans over the months March, April and May. Thus, as the vernal equinox is not set to the beginning of a month, the starting day needs to be shifted from 21 March to 1 April. Since the number of days in between these points on the orbit might differ for other time periods, the shift needs to be defined by the angle between today's 21 March and 1 April rather than the time passed. Then, the starting points of the other months will be calculated by increasing the true anomaly by 30° for each month and computing the time needed to traverse this 30° section along the orbit.

The duration of a month will usually not be an integer, but a decimal number. To deal with this, the "largest remainder method" is applied: first, each month is allotted its integer part of the number of days it encompasses. As some days are still left over afterwards, the months are then ranked by their largest fractional remainders. Finally, the unallocated days are allotted to the months according to the ranking until there are none left. After the length of the months are computed for the angular calendar, the last step is to calculate monthly means.

The calendar correction was also applied to the Pre-Industrial simulation output, as there are slight differences between the modern and the angular calendar. Table 3.2 shows the computed number of days in all the months for 1850CE (PI) and for 127 000 BP (LIG) (after Shi et al., 2022).

Table 3.2: Length of months and seasons (in days) for the modern Gregorian calendar and for the angular calendar during PI and LIG, computed using the routine `calendar.py` (`https://gitlab.awi.de/xshi/calendar`).

Month/Season	Gregorian	PI angular	LIG angular
January	31	29	33
February	28/29	30/31	32/33
March	31	30	31
April	30	31	30
May	31	31	29
June	30	31	28
July	31	31	28
August	31	31	29
September	30	31	29
October	31	30	31
November	30	30	32
December	31	30	33
Boreal winter	90	89	98
Boreal spring	92	92	90
Boreal summer	92	93	85
Boreal autumn	91	91	92

4 Results

In the following section, the results of the climate model simulations will be shown. First, changes in large-scale patterns between the LIG and PI in both, atmosphere and oceans, will be examined. Then, additional focus will be laid on the climate in the North Atlantic region and Arctic sea ice. In the following, mostly seasonal means will be evaluated, using the meteorological definition of seasons: NH winter includes December, January and February (DJF), NH spring March, April and May (MAM), NH summer June, July and August (JJA) and NH autumn consists of September, October and November (SON).

4.1 Large-scale patterns

To examine how the changes in orbital parameters affect the seasonality during the LIG, the incoming solar radiation at the top of the atmosphere (TOA insolation), the surface air temperature and the precipitation are of great interest. They were analysed with regard to changes in their seasonal means compared to the PI. Additionally, the impact of the choice of calendar will be evaluated. Finally, we will move from the atmosphere to the ocean and evaluate the simulated sea surface temperature and sea surface salinity, again with a focus on seasonal means and how they are affected by the choice of calendar.

4.1.1 Insolation

The TOA insolation is directly related to variations in obliquity, eccentricity and precession, and is an important driver of climate change. Particularly interesting is the latitudinal distribution of the monthly mean TOA insolation because the orbital parameters do not affect all latitudes and seasons equally. For this purpose, the insolation was averaged monthly and along the latitudes. Figure 4.1 shows the anomalies between the LIG and PI TOA insolation.

The effect of the calendar correction is immediately apparent: the latitudinal distribution of insolation using the uncorrected classical calendar (Figure 4.1 (a)) shows a temporal shift between NH and SH insolation extremes, particularly for the

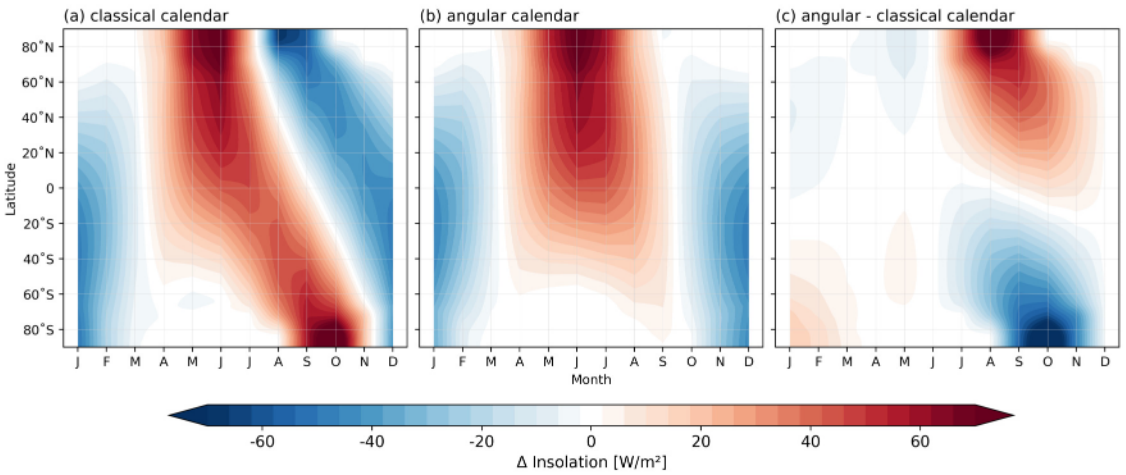

Figure 4.1: Latitudinal distribution of the monthly mean TOA insolation [W/m^2]: (a) LIG minus PI insolation anomalies using the classical Gregorian calendar, (b) LIG minus PI insolation anomalies using the angular calendar, (c) LIG–PI angular anomalies minus LIG–PI classical anomalies.

second half of the year. By contrast, the calendar-corrected distribution of insolation (Figure 4.1 (b)) shows a more symmetrical pattern.

For the calendar-corrected model output, the strongest insolation anomalies between LIG and PI occur during JJA and DJF. From MAM until the beginning of SON, there are positive insolation anomalies everywhere except for the SH polar region. This indicates more incoming solar radiation in the LIG compared to the PI. The strongest positive anomaly occurs in June in the Arctic regions, with roughly 74 W/m^2 additional insolation compared to the PI. In SON and DJF, less insolation reaches the SH as well as the NH tropics and mid-latitudes, particularly in December to January when the deficit in insolation amounts to roughly -50 W/m^2.

Figure 4.1 (c) shows the differences between the LIG–PI anomalies for the corrected (angular calendar) and the uncorrected (classical calendar) insolation means. The biggest differences occur for high latitudes. In August, the TOA insolation is severely underestimated if no calendar correction is applied. With a calendar correction, the Arctic region receives around 88 W/m^2 more TOA insolation than without correction. For the SH, there is a strong negative anomaly, amounting to a difference of -95 W/m^2 between the corrected and the uncorrected model output in the SH polar regions.

4.1.2 Surface air temperature

The surface air temperature shows strong deviations over land between the LIG and the PI, particularly in JJA and DJF (see Figure 4.2). Negative temperature anomalies indicate a cooling in the LIG compared to the PI, positive anomalies a warming.

In DJF, cooling is observed over all continents and oceans, except for the Arctic and the Southern Ocean. The cooling is especially strong over Northern Africa, India and South Asia. In MAM, the temperature anomalies show a similar pattern, but the cooling is less pronounced. Positive temperature anomalies appear over Greenland, Siberia and Antarctica. Slight warming during both of these seasons can also be seen in some smaller regions over the oceans, namely in the northeastern Pacific, at the west coast of Africa and in the North Atlantic south of Greenland. In JJA and SON, the calendar-corrected SAT anomalies show warmer temperatures for the LIG than for the PI almost everywhere. The only regions showing colder temperatures are the Sahel region, India, and some regions over the SH tropical oceans. The strongest warming in JJA occurs over the NH continents, reaching more than +8 °C. During SON, there are also strong positive temperature anomalies occurring over the Arctic region. Without the calendar correction, these are much less pronounced. In addition, the uncorrected SAT anomalies over NH continents show a slight cooling instead of a warming for SON.

The paleo calendar effect can best be observed in Figure 4.2 (i) - (l), which show the differences between the calendar-corrected and the uncorrected SAT anomalies. Positive temperature differences indicate more positive SAT anomalies for the corrected, angular calendar, meaning that without correction, the SAT anomalies are underestimated. Negative anomalies imply overestimation of SAT anomalies for the uncorrected data.
Because the date of perihelion is fixed to 21 March, the calendar effect is small for MAM and reaches its maximum in SON. Without the calendar correction, the temperatures during SON are severely underestimated for the NH continents, with the temperature anomalies reaching +6 °C. This is visible in Figure 4.2 (d), where

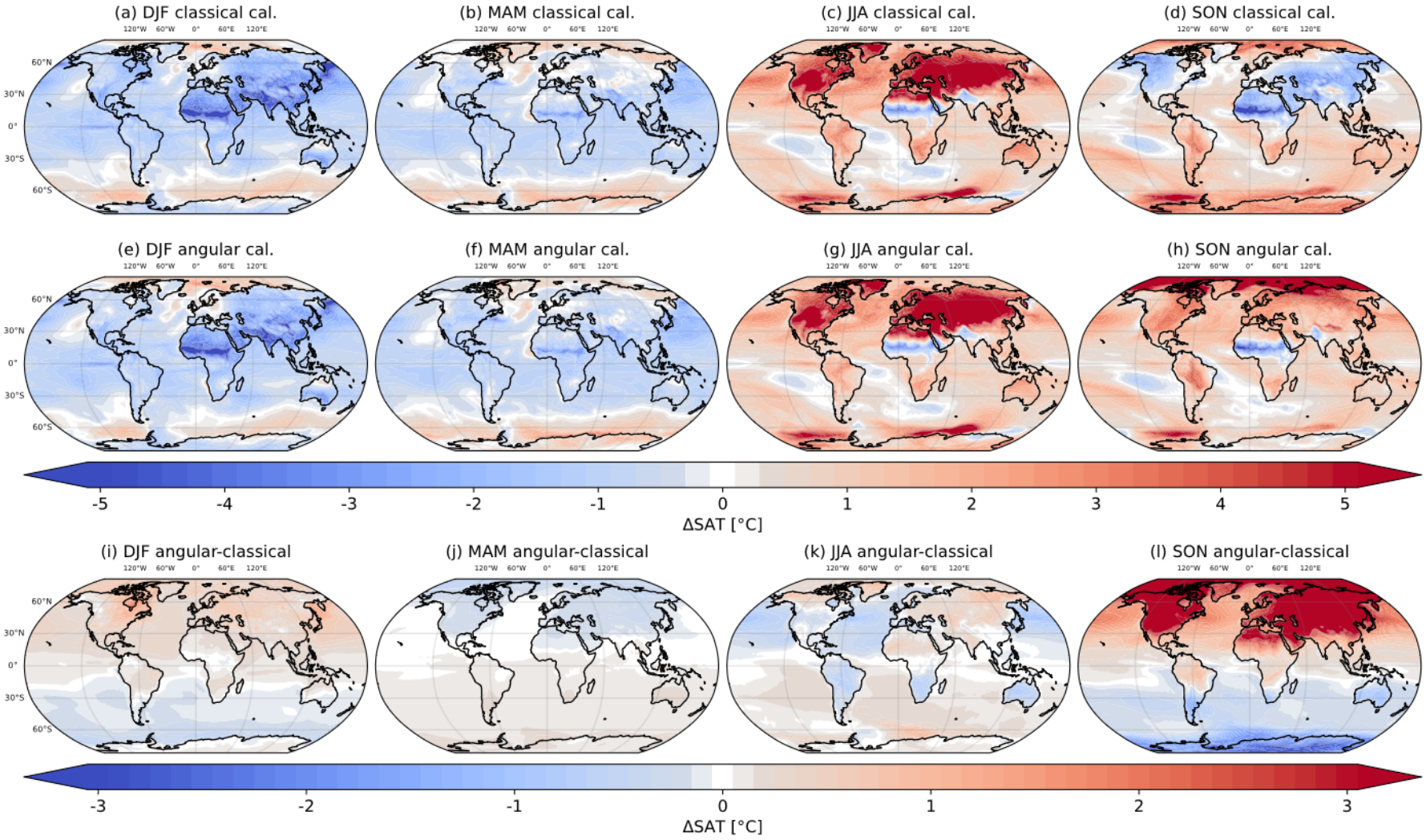

Figure 4.2: Seasonal mean 2m air temperature anomalies LIG minus PI (a)-(d): classical calendar, (e)-(h): angular calendar, (i)-(l): LIG–PI angular calendar minus LIG–PI classical calendar (please note the different scales).

for the classical calendar, the NH land temperatures are colder compared to the PI, whereas for the angular calendar (Figure 4.2 (h)) warming is observed, meaning that the signs are even reversed between the two different calendars. For the SH on the other hand, the temperature increase in SON is overestimated, especially over the mid- and high latitudinal continents. In the other seasons, the temperature deviations between the two calendars are much smaller. In DJF, the classical calendar slightly overestimates the cooling over land, and the warming over the Southern Ocean. MAM shows the biggest agreement between the calendars, with only very little warming and cooling occurring on the SH and the NH respectively. In JJA, after the calendar correction, warmer temperatures are observed over NH land and SH oceans, and colder temperatures on the SH continents, except for Antarctica, and over the NH oceans.

4.1.3 Precipitation

Changes in precipitation patterns can largely influence temperature, humidity and the water cycle. Further, it has a significant impact on ecosystems, for instance by promoting or restricting the growth of vegetation. Hence, changes in monthly mean precipitation between LIG and PI were analysed. The results show that differences in precipitation between LIG and PI are mostly concentrated around the tropical rain belt (see Figure 4.3). Positive precipitation anomalies indicate an increase in precipitation in the LIG compared to the PI, negative anomalies show a decrease.

In DJF, a southward shift of the ITCZ is perceptible over the tropical Atlantic, marked by stronger precipitation south of the Equator and less precipitation around the Equator. South America, Southern Africa and Australia receive less precipitation during this time, indicating weaker summer monsoons on the SH. In MAM, there are only comparatively small precipitation anomalies that mostly affect the tropical oceans, where precipitation is slightly decreased. Over central Africa and Indonesia, precipitation is slightly increased.

Stronger anomalies occur in JJA and SON, when a northward shift of the ITCZ is observed. It is marked by stronger precipitation over the NH tropical Atlantic and weaker precipitation around the Equator. The African and Asian summer mon-

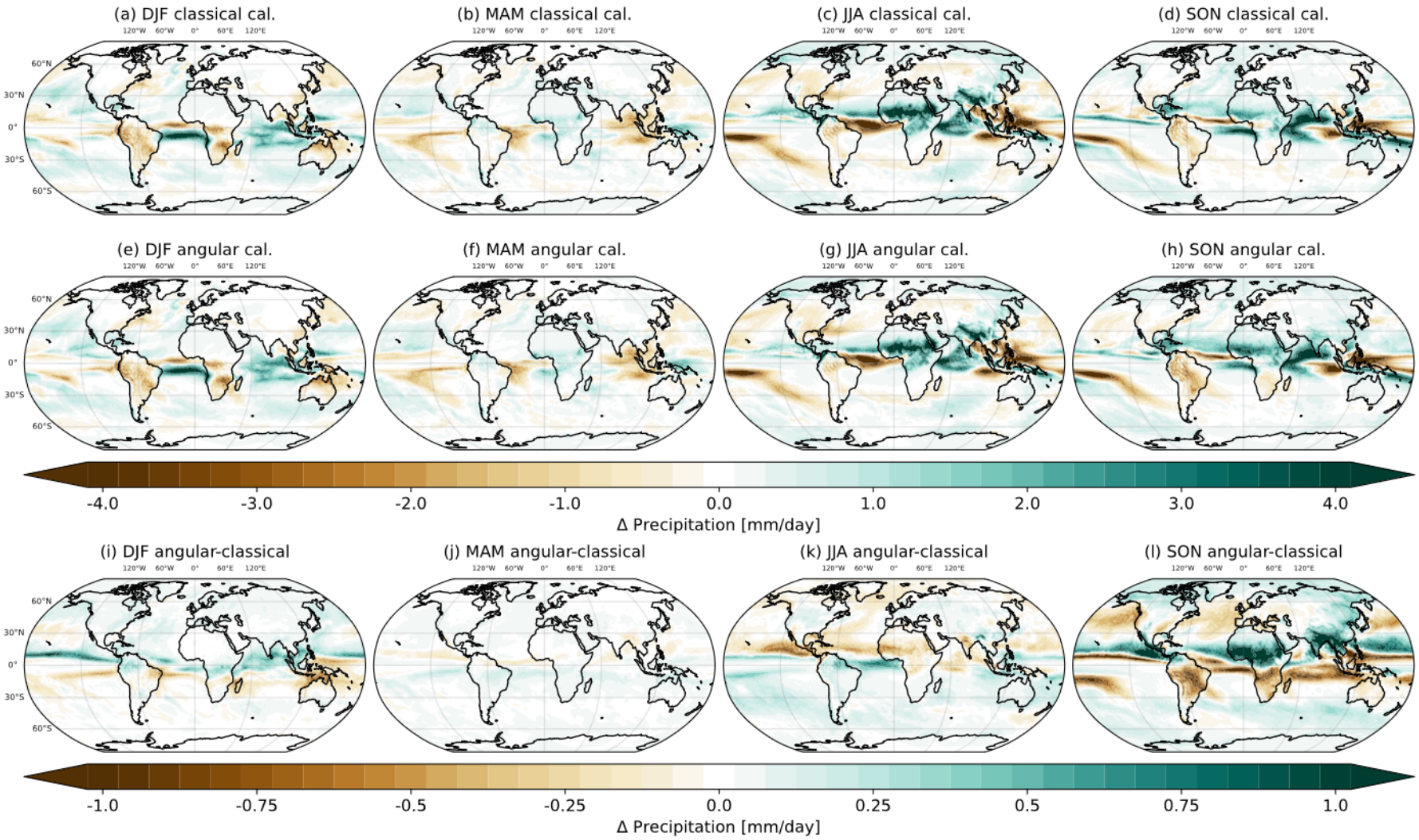

Figure 4.3: Seasonal mean precipitation anomalies LIG minus PI (a)-(d): classical calendar, (e)-(h): angular calendar, (i)-(l): LIG–PI angular calendar minus LIG–PI classical calendar (please note the different scales).

soons are stronger in the LIG than the PI, marked by stronger precipitation over Africa, India and Southeast Asia. Increased precipitation also occurs over most of the Indian Ocean, Indonesia and Central America. Over the SH tropical Pacific, it is drier in the LIG compared to the PI and, especially in JJA, there is also drying over the northeastern Pacific and North America. South America is also affected by drying in these seasons, most notably in SON. Likewise, some regions in Southeast Asia and over the southeastern Indian Ocean receive less precipitation during JJA and SON.

In agreement with the results for the surface air temperature, the paleo calendar effect for the precipitation (Figure 4.3 (i) - (l)) is strongest in SON. Without the calendar correction, the northward shift of the ITCZ in SON is underestimated, indicated by negative anomalies between the angular and the classical calendar around and south of the Equator, and positive anomalies north of it. The classical calendar also underestimates the increase in precipitation over North Africa and South Asia, marked by positive anomalies in these regions. Finally, negative precipitation anomalies over the NH Pacific as well as over South America and Southern Africa indicate that the drying of these places is underestimated in the uncorrected model output. In DJF, the classical calendar slightly underestimates the increase in precipitation around the Equator and the decrease south of it. In MAM, the paleo calendar effect is very minor, showing a slightly increased precipitation south of the Equator when model output is calendar-corrected, and decreased precipitation north of it. JJA exhibits a similar pattern to DJF, but with reversed signs: with the calendar correction, there is less precipitation in the NH tropical regions and more precipitation around and south of the Equator compared to the uncorrected model output.

4.1.4 Sea surface temperature

The changes in seasonal mean sea surface temperature (SST) in LIG compared to PI (Figure 4.4) show similar patterns as the SAT over oceans.

In DJF and MAM, the SST anomalies are predominantly negative, indicating a

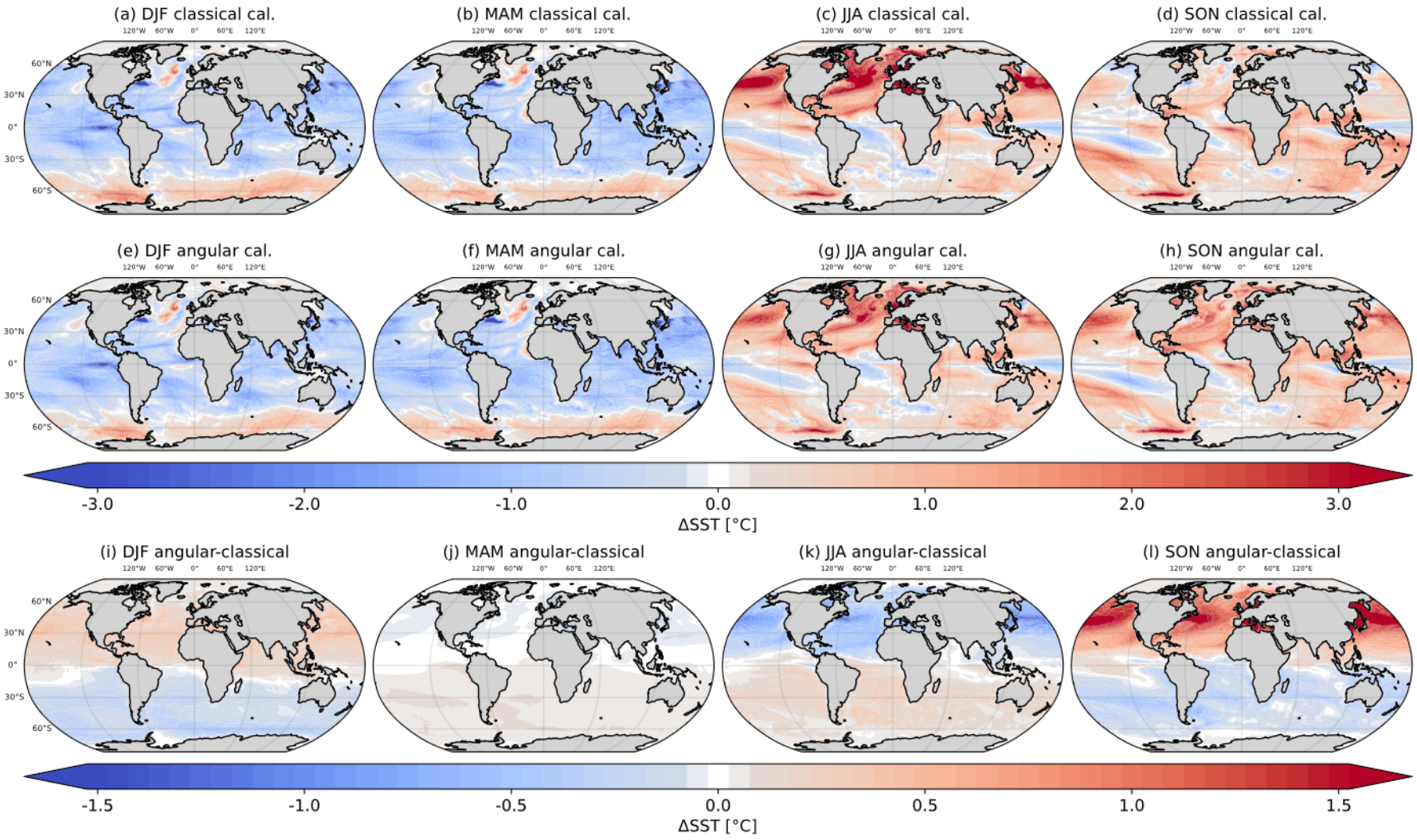

Figure 4.4: Seasonal mean sea surface temperature anomalies LIG minus PI (a)-(d): classical calendar, (e)-(h): angular calendar, (i)-(l): LIG–PI angular calendar minus LIG–PI classical calendar.

cooling in the LIG compared to the PI. Positive anomalies, and thus a warming in the LIG, can be observed in the Southern Ocean and, less pronounced, in the Arctic Ocean. Further, warming also occurs in some smaller regions of the Atlantic Ocean and around the western coast of North America. In the North Atlantic, a dipole pattern is observed: close to the east coast of North America, there is a cooling, while northeast of this is a region of relative warming in the LIG SSTs. This pattern can also be observed in the SAT anomalies, but to a lesser extent. Warmer SSTs also occur along the western coasts of Europe, Northern and Southern Africa.

In JJA, positive SST anomalies predominate. The warming is strongest in the NH mid-latitudes, reaching up to $+4.5\,°C$ for the calendar-corrected data. The NH subtropics and the Arctic Ocean also show a slight warming. On the SH, the SSTs show a mix of warming and cooling, with the cooling mostly occurring in the tropical and subtropical oceans. When compared to the precipitation anomalies, it is noticeable that the negative SST anomalies occur in regions of relative drying compared to the PI.

In SON, the SST anomalies on the SH look very similar to those in JJA. On the NH however, the warming is less pronounced than in JJA, and some regions in the North Atlantic and North Pacific exhibit a cooling. Further, there are distinct differences between the calendar-corrected (Figure 4.4 (h)) and the uncorrected (Figure 4.4 (d)) model results in SON: the NH oceans are noticeably warmer if a calendar correction is applied. The colder spots observed in both the North Atlantic and North Pacific are decreased in size and less distinct, and warming in the mid-latitudes is more pronounced.

Overall, the paleo calendar effect for the SST anomalies is highly consistent with that for SATs. In MAM and JJA, negative SST anomalies occur on the NH, indicating that SST anomalies between LIG and PI are overestimated without a calendar correction. On the SH by contrast, the SST anomalies are underestimated. This effect is very small for MAM, but stronger for JJA. Both in SON and DJF, the pattern is reversed, meaning SST anomalies are underestimated for the NH and overestimated for the SH when using the classical Gregorian calendar. As before,

the paleo calendar effect is most pronounced in SON. In the NH mid-latitudes, it reaches a maximum of +2.8 °C compared to the uncorrected SST anomalies.

4.1.5 Sea surface salinity

Sea surface salinity (SSS) can act as an indicator for changes in ocean currents, climate patterns and the global water cycle. Figure 4.5 shows the seasonal mean SSS anomalies between LIG and PI.

Most regions show similar patterns year-round with only slight variations in amplitude between the seasons. In the tropics and subtropics, the salinity mostly shows similar patterns to the precipitation anomalies (Figure 4.3): in regions where precipitation is amplified (weakened) during the LIG, the SSS is reduced (increased) due to the additional (reduced) freshwater input. For instance, this can be observed in the northwestern part of the Indian Ocean, where negative SSS anomalies occur, indicating a reduced salinity in the LIG compared to the PI. In the eastern part of the Indian Ocean, the salinity is increased. In regions of weakened precipitation during the LIG in the western equatorial Pacific, the SSS shows an increase. However, the negative precipitation anomalies only occur in JJA and SON, whereas the positive SSS anomalies are observable year-round but are strongest in JJA and SON.

In the region of the Benguela Current along the west coast of Africa, and in the SH tropical Atlantic, the SSS is reduced. The SSS reduction along the African coast is accompanied by warmer SSTs in this region.

In the North Atlantic, the dipole pattern along the east coast of North America that is also visible in the SAT and SST anomalies can also be observed in the SSS anomalies. Along the coast, where the water is colder, it is also less saline, while the warmer water further away from the coast is more saline.

The Arctic Ocean shows a decreased SSS almost everywhere, most notably in JJA and SON. This is likely due to an increased freshwater input by melting ice. Only on the Siberian Coast in the Kara Sea, the salinity is increased in the LIG.

The Mediterranean Sea shows a strong freshening which is most likely related to the amplified North African monsoon and the associated increased freshwater input from the Nile river.

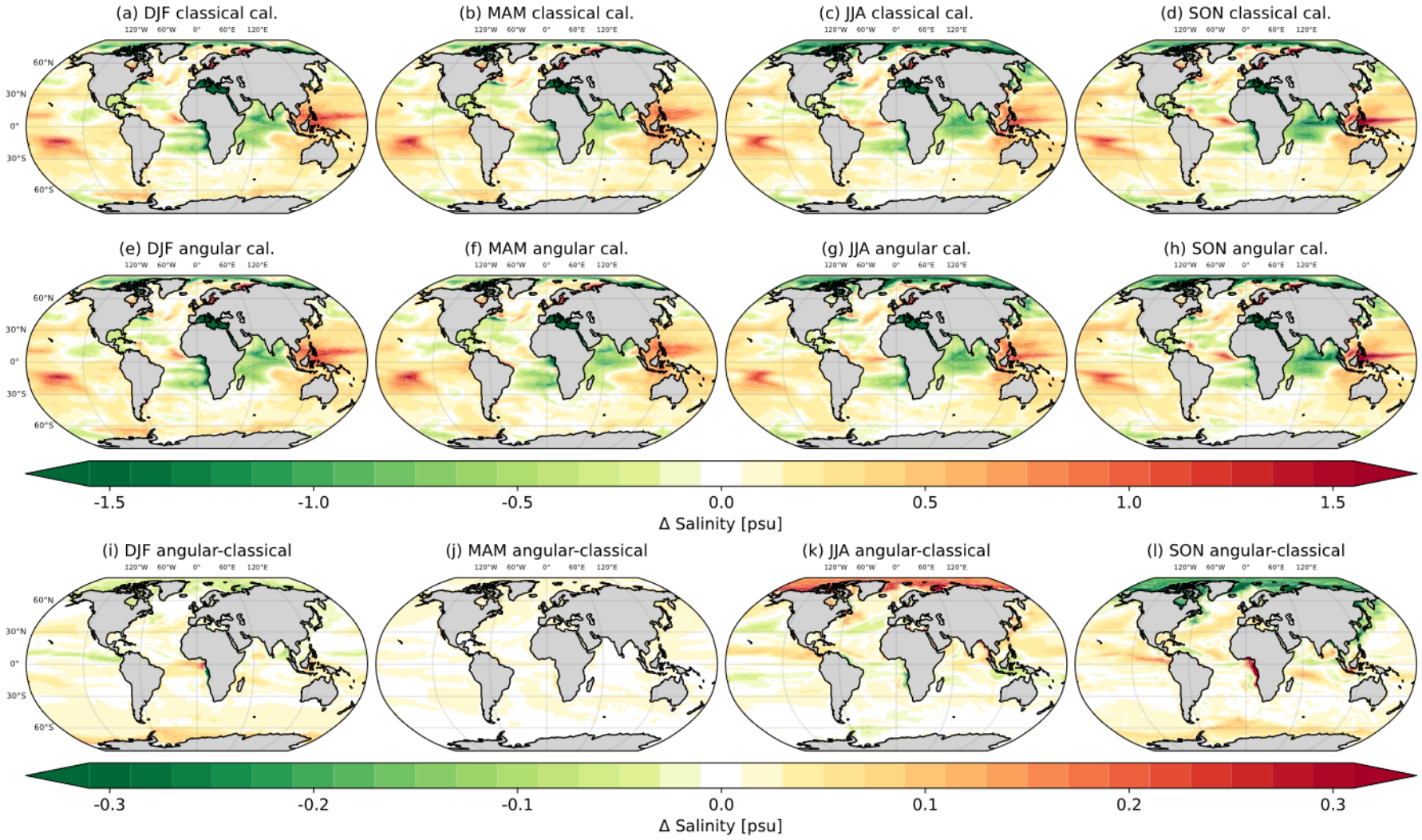

Figure 4.5: Seasonal mean sea surface salinity anomalies for LIG minus PI; (a)-(d): classical calendar, (e)-(h): angular calendar, (i)-(l): LIG–PI angular calendar minus LIG–PI classical calendar (please note the differing scales).

The paleo calendar effect for the SSS anomalies is depicted in Figure 4.5 (i) - (l). Positive anomalies indicate a higher salinity in the calendar-corrected output, meaning it is underestimated without calendar correction. Negative anomalies imply an overestimation of the SSS anomalies for the uncorrected model results. In DJF, there are only slight, predominantly positive differences between the two applied calendars. In the Arctic Ocean, negative anomalies occur, showing that the SSS is overestimated using the Gregorian calendar. Along the Equator, where precipitation and consequently freshwater input is underestimated, so is the salinity. Finally, on the west coast of Africa, there is a small region where SSS is underestimated, whereas south of this it is overestimated. Differences in MAM are negligible. In JJA, the salinity is underestimated in the Arctic Ocean. In the tropics and subtropics, both slightly positive and negative anomalies occur, aligning with the precipitation anomalies in these regions. The North Atlantic exhibits a positive anomaly in the area of the before mentioned dipole pattern, and east of this a negative anomaly coinciding with an area of overestimated precipitation. In SON, the salinity anomalies between LIG and PI are overestimated without calendar correction, and underestimated along the west coast of Africa. The pattern in the North Atlantic is reversed compared to JJA.

4.2 North Atlantic climate and Arctic sea ice

As mentioned before in Section 2.2, the extent of Arctic summer sea ice during the LIG is much debated. For this reason, it was also investigated in the scope of this thesis. Additionally, the importance of a calendar correction on the analysis of Arctic sea ice will be examined. Further, differences between LIG and PI climate over the Arctic region and how they are affected by the choice of calendar will be analysed.

4.2.1 Arctic sea ice

Sea ice concentration. Figure 4.6 shows the sea ice concentration (SIC) in March and in September for the LIG, as well as the SIC anomalies between LIG and PI.

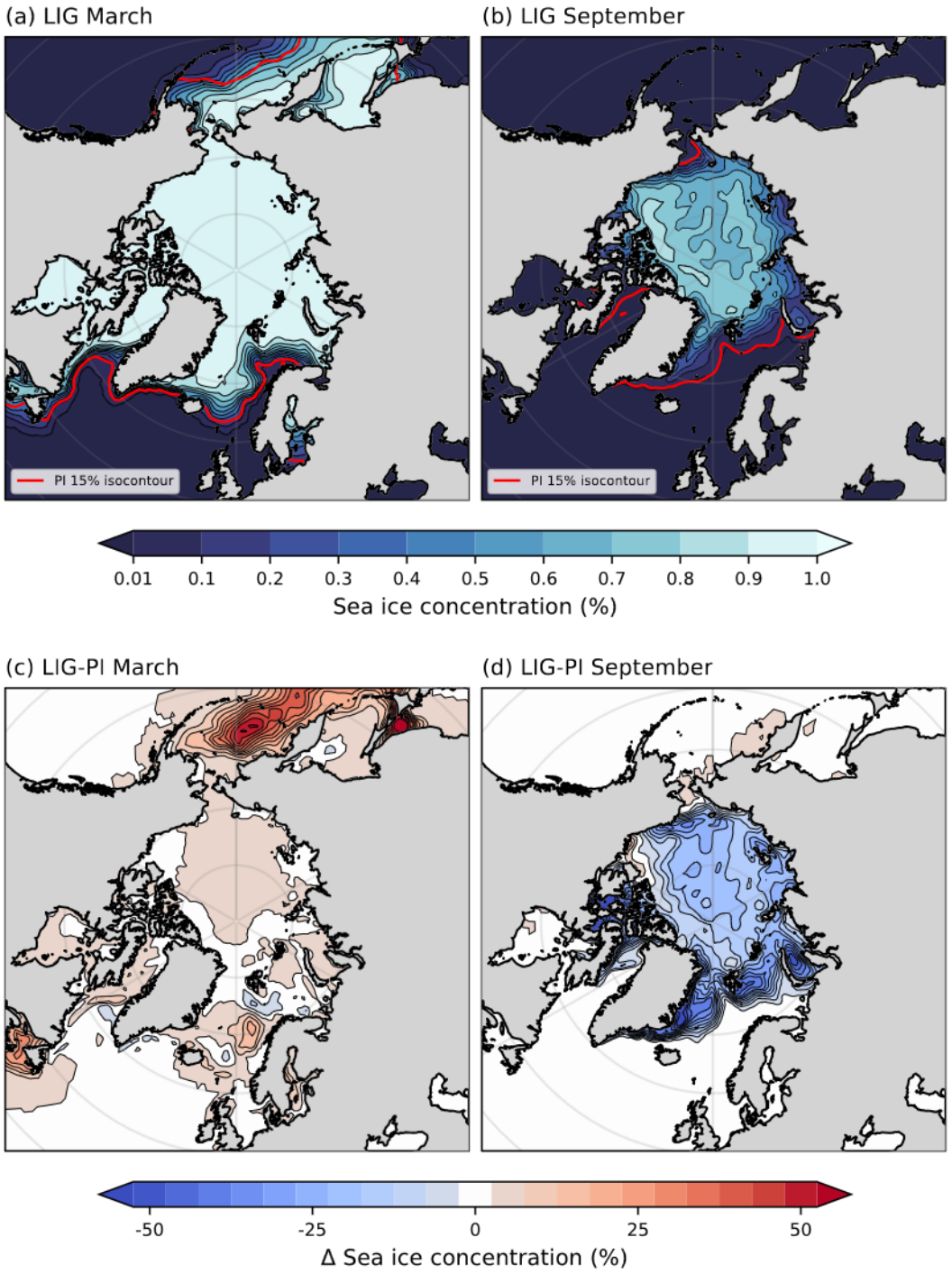

Figure 4.6: Arctic sea ice concentration (calendar-corrected) (a) LIG March sea ice concentration, red line marks 15% PI isocontour; (b) LIG September, red line marks 15% PI isocontour; (c) LIG–PI sea ice concentration anomalies; (d) LIG–PI September anomalies.

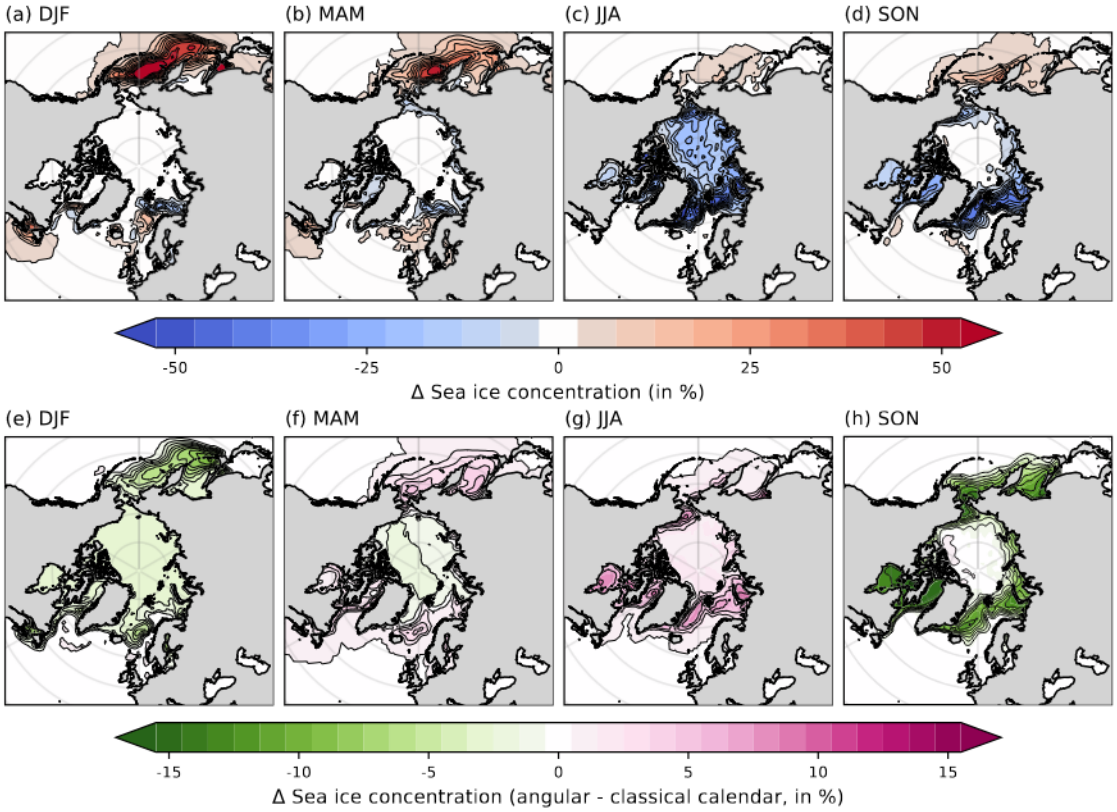

Figure 4.7: Seasonal sea ice concentration anomalies. (a) - (d): LIG – PI anomalies, (e) - (h): differences between angular and classical calendar.

Positive anomalies are marked in red, indicating an increased SIC for the LIG, while a decrease is depicted in blue. In March, the SIC predominantly shows an increase during the LIG compared to the PI. In the Central Arctic Ocean, it is mostly unvaried or slightly increased. In the Baffin Bay and the Hudson Bay, SIC is also increased, as well as in the transition zone from Atlantic Ocean to Arctic Ocean. The most significant increase is observed in the Bering Sea. A slight decrease can be seen south of Greenland and south of Svalbard.

In September, there is a significant decrease in SIC during the LIG, especially at the sea ice margins. Along the eastern coast of Canada and Greenland, southeast of Svalbard and in the Kara Sea, the decrease in SIC is most distinct. The only areas showing a slightly higher SIC are the Bering Sea, a small region on the Canadian coast in the eastern part of the Beaufort Sea, and a few small spots in the Hudson Bay. In the LIG, the SIC is highest in regions north of Greenland and the Canadian coast.

Figure 4.7 shows the seasonal means of the SIC anomalies for LIG minus PI and the differences between the calendar-corrected and the uncorrected results. Variations in SIC mostly occur at sea ice margins. In DJF, there is a significant increase in SIC in the Bering Sea during the LIG. Around the coasts of western North America, southern Greenland, and north of Scandinavia, some regions show an increase, others a decrease in SIC, but the changes are relatively minor. The deviations between angular and classical calendar show negative anomalies, indicating that the SIC during the LIG is overestimated for the classical calendar, most notably in the Bering Sea. The anomalies in SIC during MAM look similar to DJF, but the increase in the Bering Sea is less pronounced and there is a decrease in SIC west of Greenland that was not observed in DJF. The paleo calendar effect shows an overestimation of LIG SIC in the Central Arctic Ocean and an underestimation in the oceans surrounding it. JJA is the only season in which changes in the SIC occur in the Central Arctic. It shows a decrease compared to the PI that extends and enhances towards the sea ice margins along the North Atlantic. In the Bering Sea, a slight increase in SIC is observed. The calendar effect shows an underestimation of SIC in the whole Arctic

region, which is again most pronounced at the sea ice margins. In SON, the pattern of SIC anomalies looks similar to JJA, except for the Central Arctic Ocean, where no anomalies are observed. Without calendar correction, the anomalies are strongly overestimated, particularly in the Hudson Bay and the Baffin Bay, as well as in the Bering Strait.

September sea ice area time series. The temporal evolution of Arctic sea ice area in September was analysed to see whether its variability differed in a meaningful way and if the choice of calendar has a significant impact on sea ice area. Figure 4.8 shows the progression of September sea ice area over 200 simulation years for the LIG and PI, and the sea ice area anomalies between LIG and PI. To extend the time series beyond the 40 years that were simulated in the scope of this thesis, additional 160 years were taken from the simulations they were branched off from. These PI and LIG simulations were much longer, spanning 700 and 1000 years, respectively. But as the SAT in the Arctic region does not show significant variability (see Figure A.1), indicating that the simulations are in quasi-equilibrium, only the last 160 years of the simulations were used. The extension of the time series was done as sea ice often exhibits multi-decadal variability that could not sufficiently be discerned in a time series spanning only 40 years. However, the calendar-correction was solely applied to the last 40 years of the LIG–PI anomalies, as this shorter simulation produced daily data, whereas for the longer simulation only monthly means were saved and the calendar-correction for monthly data is not as straightforward.

A 15-year rolling-mean was applied to accentuate the multi-decadal variability. Both the LIG and the PI simulations exhibit intra-decadal and multi-decadal variability that does not significantly differ between the two periods (see Figure 4.8a). During the PI, the modelled September sea ice area, with a 15-year rolling mean applied, fluctuates approximately between $10 \times 10^6\,\mathrm{km}^2$ and $11 \times 10^6\,\mathrm{km}^2$. The LIG September sea ice area is lower, fluctuating between $8 \times 10^6\,\mathrm{km}^2$ and just above $9 \times 10^6\,\mathrm{km}^2$, after applying a 15-year rolling mean. Without application of a rolling mean, there are some outliers outside of these ranges for both LIG and PI.

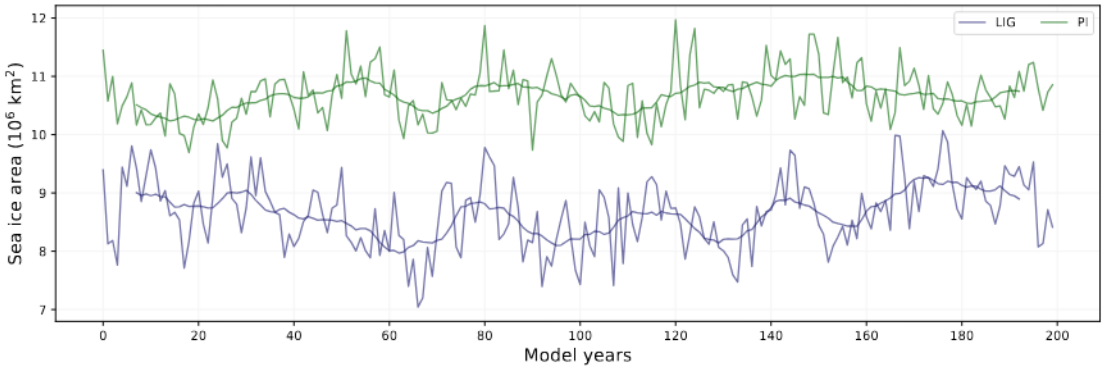

(a) Simulated September sea ice area for LIG and PI. The green line marks the results (and 15-year rolling mean) of the PI simulation, blue the LIG simulation.

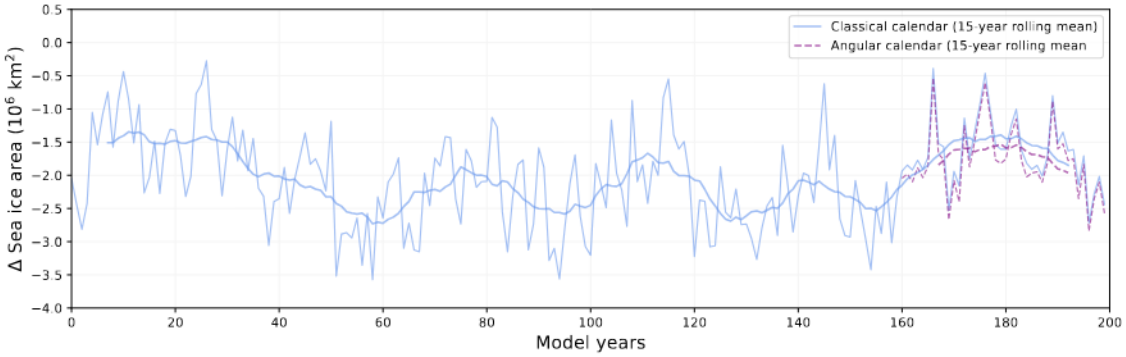

(b) LIG – PI September sea ice area anomalies. The blue line depicts the simulated sea ice area and its 15-year rolling mean without calendar correction, the dashed purple line marks the calendar-corrected results (and 15-year rolling mean).

Figure 4.8: September sea ice area simulated over 200 years. The last 40 years are taken from the simulations featured in this thesis, additional 160 years were added from the simulations they were branched off from.

Figure 4.8b shows the anomalies between the LIG and PI September sea ice area. The averaged time series ranges between $-2.7 \times 10^6\,\mathrm{km}^2$ and $-1.3 \times 10^6\,\mathrm{km}^2$, approximately. For the last 40 model years, the calendar-corrected anomalies are shown, as well. They are slightly below the uncorrected anomalies, meaning without correction, the September sea ice area during the LIG is greater and therefore overestimated. However, this effect is small. The differences between both curves are only roughly $0.1 \times 10^6\,\mathrm{km}^2$ to $0.2 \times 10^6\,\mathrm{km}^2$.

4.2.2 The paleo calendar effect on North Atlantic climate

Since warming is most pronounced in the NH mid- to high latitudes during the LIG due to Arctic Amplification, additional focus was placed on the paleo calendar effect in the Arctic region. Figure 4.9 depicts the LIG–PI anomalies in SAT, precipitation, SST and SSS over the Arctic region. The corresponding paleo calendar effect is shown in Figure 4.10.

In DJF, the SAT anomalies mostly show a cooling in the LIG. The Central Arctic Ocean however exhibits positive SAT anomalies, indicating a warming. A slight warming is also observed over the North Atlantic and northern Europe. Over the North Atlantic and North Pacific, warmer temperatures are accompanied by an increase in precipitation during the LIG, and colder temperatures by a decrease. Over the Arctic Ocean, there are no marked changes in precipitation. The SST anomalies show similarities to the SAT anomalies, however there is very little to no warming in the Arctic Ocean. In the North Atlantic, there are additional regions where warmer temperatures occur, namely south of Greenland and west of northern Canada. The salinity predominantly shows changes in the Arctic Ocean, where it is decreased during the LIG, most notably along the coasts and the transition of Atlantic to Arctic Ocean. An increase in salinity occurs in the Kara Sea, in the Baltic Sea and in the Hudson Bay. The paleo calendar effect causes a relatively uniform underestimation of SAT and SST anomalies when no calendar correction is conducted. Precipitation anomalies are also mostly slightly underestimated, whereas salinity anomalies are overestimated in the Arctic Ocean.

In MAM, similar patterns to those in DJF are observed for the LIG–PI anomalies. For the SAT anomalies, differences occur over Greenland and northeast Russia, which show a slight warming, and the Arctic Ocean, which exhibits cooling north of Canada. The precipitation anomalies indicate a drying along the west coast of North America. The SST and SSS anomalies show only marginal changes compared to DJF. The calendar effect in MAM deviates from that in DJF, however. Only slight differences occur between the calendars, but contrary to DJF, the SAT and SST anomalies are colder using the angular calendar. Precipitation and salinity are increased by a little bit, but are relatively uniform over the whole area.

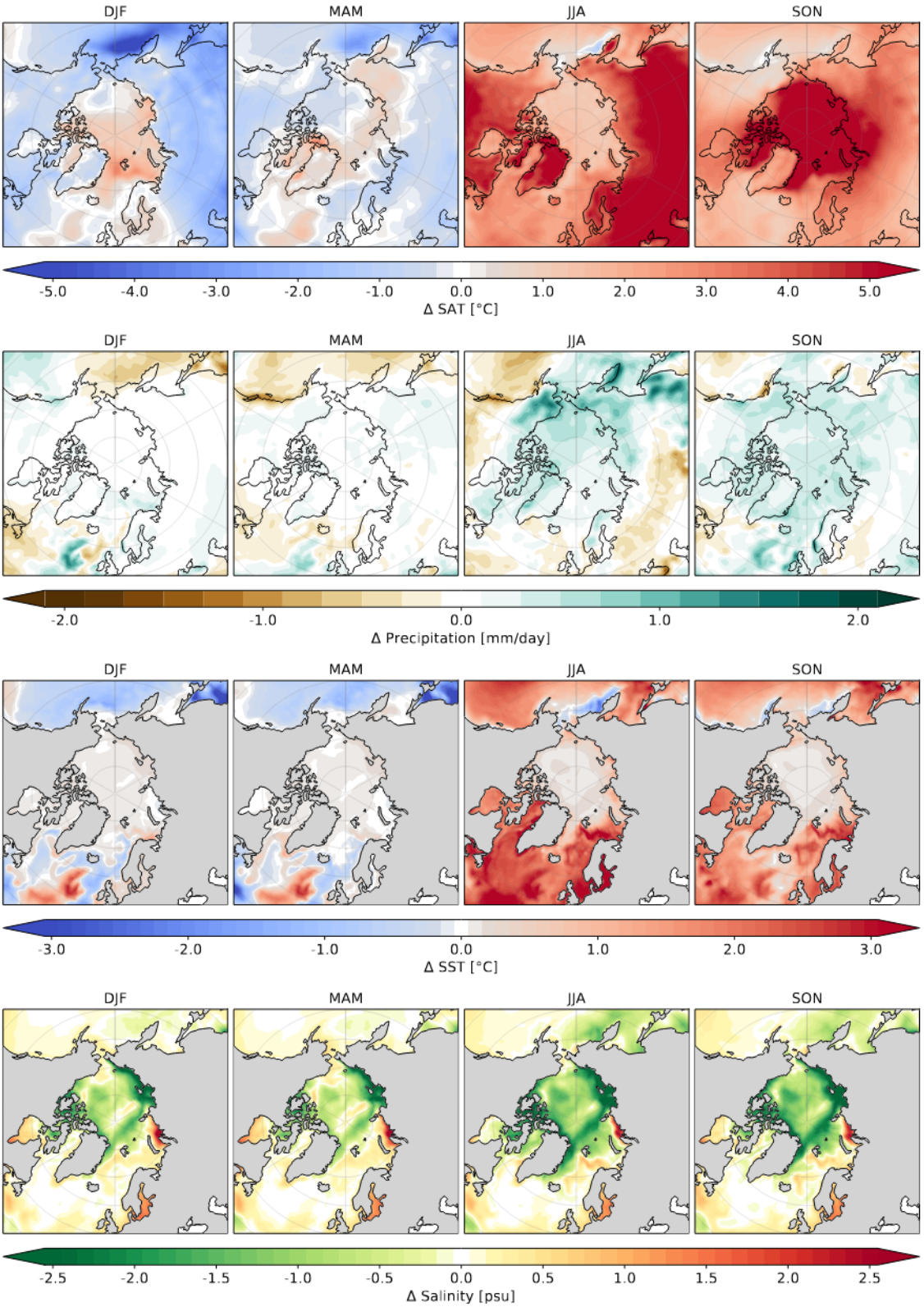

Figure 4.9: Seasonal mean LIG – PI anomalies over NH high latitudes. From top to bottom: surface air temperature, precipitation, sea surface temperature, sea surface salinity. Means were calculated using the angular calendar.

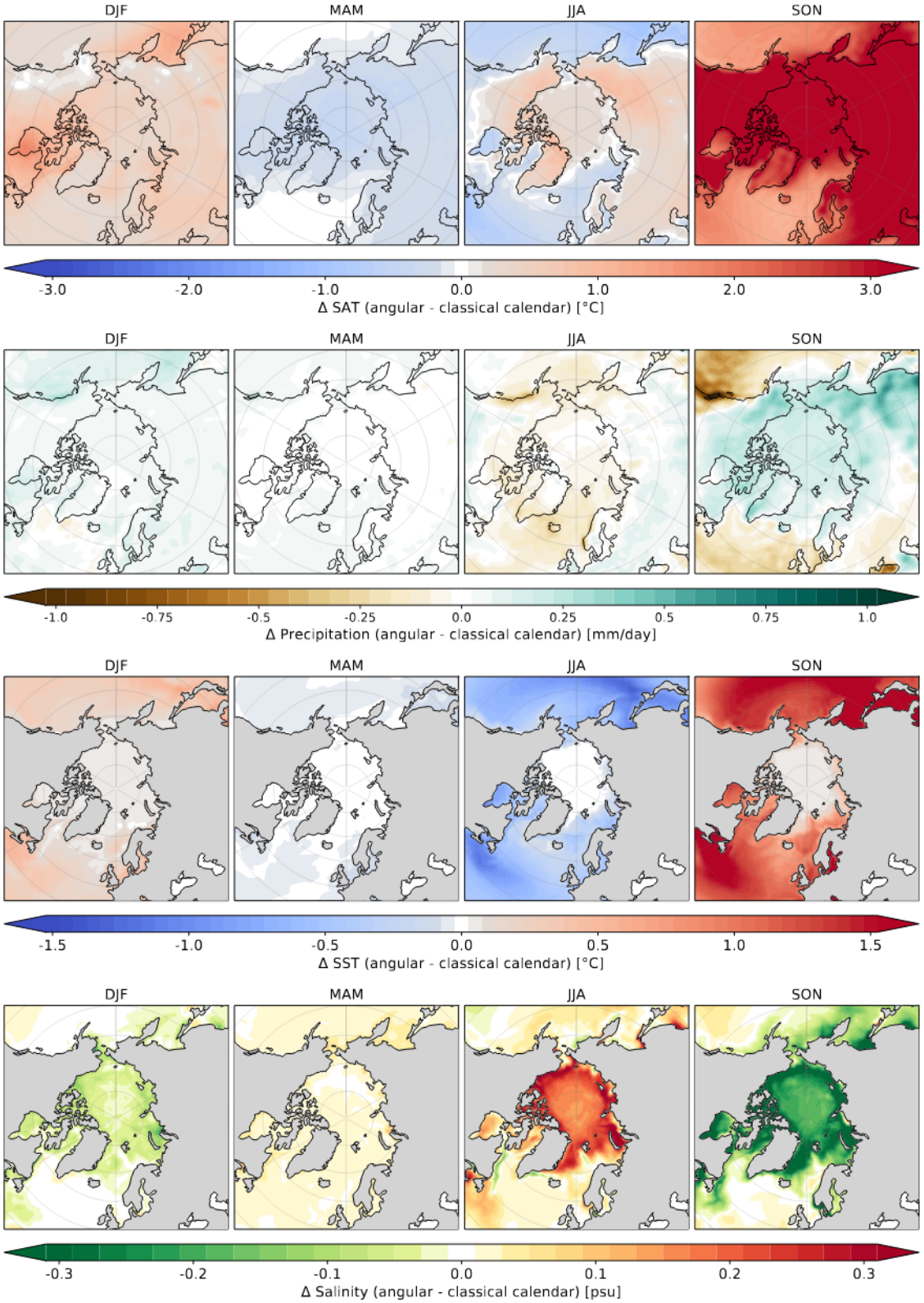

Figure 4.10: Differences between angular and classical calendar on seasonal mean LIG – PI anomalies over NH high latitudes. From top to bottom: surface air temperature, precipitation, sea surface temperature, sea surface salinity.

In JJA, strong warming, in some places exceeding 5 °C, is observed over the continents in NH high latitudes. Only on the northeastern coast of Russia is a region that is a bit colder during the LIG. The oceans also exhibit warming but it is less pronounced compared to the continents. Precipitation is increased around the Bering Strait and in the Central Arctic. Moving southwards, it decreases. The salinity anomalies are comparable to those observed before, but the decline in the Arctic Ocean is more pronounced and extends further south towards Greenland and also to the Bering Sea. Without application of a calendar correction, the SAT anomalies are underestimated over the Central Arctic and the high latitude continents, and overestimated over the North Atlantic and Pacific. Precipitation is mostly overestimated over the oceans and underestimated over land. The SST is overestimated without calendar correction, only in the Central Arctic it is unchanged. The salinity shows strong positive anomalies in the Arctic Ocean, meaning the classical calendar underestimates it in JJA.

The biggest SAT anomalies over the Arctic Ocean occur in SON and are similar in magnitude as the SAT anomalies over high latitude continents in JJA. The SAT anomalies over oceans and continents are decreased compared to JJA, but they still indicate a warming relative to the PI of several degree Celsius. SST anomalies are also slightly less pronounced than in JJA, but otherwise similar. Precipitation is mostly increased, especially over the Arctic Ocean and land. Salinity anomalies hardly deviate from the JJA anomalies. The differences between angular and classical calendar are greatest in SON, as before. There are very strong positive SAT and SST anomalies over all of the NH high latitudes, meaning the classical calendar markedly underestimates SAT anomalies during this season. Precipitation is underestimated over the Arctic Ocean and Greenland, northern Russia and Canada, and overestimated over the North Atlantic and North Pacific, most notably along the west coast of North America. Finally, salinity anomalies are strongly overestimated over the high latitude oceans without applying a calendar correction.

5 Discussion

Insolation. The latitudinal distribution of the monthly mean TOA insolation showed that significantly more insolation is received in JJA on the NH, especially in mid- to high latitudes. This leads to Arctic Amplification, as can be observed in NH summer temperatures. Without the application of a calendar correction, insolation is significantly underestimated from July to September on the NH, and overestimated from September to November on the SH. The reason for these deviations are the comparably shorter NH summer months during the LIG, with the result that days from subsequent months are included in the calculation of the monthly means, skewing the results. The largest deviations occur in the high latitudes, and are in the same order of magnitude as the anomalies between LIG and PI.

Surface air temperature. The SAT anomalies indicate a strong warming over land, except for the Sahel region and India, in JJA and a cooling over land in DJF during the LIG. The warming in JJA and cooling in DJF are in strong agreement with the LIG–PI insolation anomalies. The strongest JJA warming occurs for North America and Eurasia and reaches more than 8 °C. This is more than what was reported for the PMIP4 model ensemble (6 °C, Otto-Bliesner et al., 2021). The SAT anomalies also show a strong increase in temperature over the Arctic region during JJA and SON. The negative SAT anomalies over the Sahel region and India coincide with positive precipitation anomalies indicating enhanced summer monsoons in these regions. Most likely, this leads to increased cloud cover and thus less insolation reaching the surface, causing the observed cooling.

Deviations between the calendar-corrected and the uncorrected results are most pronounced in SON. This is due to the fact that the spring equinox is fixed to 21 March, and thus the paleo calendar effect is strongest around the position on Earth's orbit farthest from this, which is reached in NH autumn. Without calendar correction, the SAT anomalies over NH continents are significantly underestimated during SON, leading to reversed signs between the LIG–PI anomalies for the classical and the angular calendar. Meanwhile, SAT anomalies over the SH are overestimated. The biggest impact is observed over Eurasia, with +6 °C warming due to the calendar

correction, indicating that the paleo calendar effect is almost as big as the deviations between LIG and PI.

Precipitation. The precipitation anomalies between LIG and PI indicate enhanced NH summer monsoons over North Africa, India, and South Asia. By contrast, SH summer monsoons over South America, Southern Africa, and Australia are attenuated during the LIG. During boreal summer, the ITCZ is shifted northwards and, during boreal winter, southwards. As a consequence of the differing magnitudes of summer monsoon between LIG and PI, the NH tropics receive significantly more precipitation in boreal summer, whereas on the SH drying occurs over land in austral summer. The driver of these changes in summer monsoons is most likely the increased insolation, which leads to an enhanced temperature gradient between land and ocean, as was found in Kutzbach (1981) for the early Holocene.

If no calendar correction is applied, the northwards shift of the ITCZ in SON as well as the increase in NH summer monsoons are underestimated. Likewise, the drying of the SH in SON is underestimated. In DJF on the other hand, the southward shift of the ITCZ is overestimated.

Sea surface temperature. As mentioned before, the SST anomalies appear very similar to the SAT anomalies over the oceans, however they are mostly less pronounced. The reason behind this is the higher heat capacity of oceans compared to the atmosphere, meaning more heat needs to be taken up by the oceans to increase their temperature. A region where stronger temperature anomalies can be observed for SST rather than SAT, is the North Atlantic. Along the mid-latitudes, a dipole pattern is observed, with cooling occurring close to the North American coast and warming northeast of this. This pattern is most noticeable during DJF and MAM, but can be observed year-round. The more pronounced manifestation of this dipole pattern suggests that it originates from the ocean. It is most likely caused by a reduced meridional heat transport.

Another region where SAT and SST anomalies deviate is the Arctic Ocean: while the SAT anomalies show strong warming in SON over the Central Arctic, no significant changes occur for the SST.

The paleo calendar effect for the SST anomalies mostly exhibits the same patterns as for the SAT anomalies.

Sea surface salinity. The sea surface salinity anomalies are strongly linked to the precipitation anomalies. Especially around the tropics and subtropics, they show very similar patterns. In regions of enhanced precipitation during the LIG, salinity is commonly decreased, and increased in comparably drier regions due to additional or weakened freshwater input, respectively. Aside from this, salinity is decreased along the southern part of the African west coast. This is an upwelling region, where colder, more saline deep waters rises to the surface. The decline in salinity suggests that upwelling in this region is weakened during the LIG. In agreement with this, the SST anomalies also show a slight warming in this region. Further, the SST and the salinity anomalies show coinciding trends in the region of the North Atlantic, where a dipole pattern is observed. Along the coast, where cooling occurs, the salinity is decreased, suggesting a decline in warm, saline waters that are transported northwards from the Equator. The Arctic Ocean shows a freshening year-round which is most pronounced in JJA and SON. This can be explained by the increased melting of Arctic sea ice driven by the warmer SAT in the Arctic region. Another region that exhibits freshening during the LIG is the Mediterranean Sea. As described in Rohling et al. (2015), the intensification of the African monsoon through orbital forcing increases the runoff from North Africa into the Mediterranean, enhancing freshwater input, and leading to the sedimentation of sapropels rich in organic carbon. This was also observed in Duboc et al. (2025), where a freshening of surface waters accompanied by oxygen depletion was observed in the Mediterranean during the LIG.

The paleo calendar effect for the salinity anomalies is most pronounced in the Artic Ocean and in the upwelling region along the west coast of Africa. In the Arctic Ocean, when a calendar correction is applied, the salinity is higher in JJA and lower in SON. This suggests that using the classical Gregorian calendar, the melting of Arctic sea ice is overestimated in JJA and underestimated in SON. The upwelling region along the African west coast is more saline after calendar correction,

indicating that the decrease in salinity and with it the attenuation of the upwelling is overestimated without the correction.

Arctic sea ice. The Arctic SIC anomalies between LIG and PI show an increase in SIC in March and a decrease in September during the LIG. The increase in March is strongly pronounced in the Bering Sea, whereas in the Central Arctic, the anomalies are relatively low. In September, there is a strong decline in SIC, especially around the sea ice margins connected to the North Atlantic. This can be explained by the orbitally driven warming in the Arctic region during JJA and SON. The warming amplifies the melting of sea ice in the NH summer, which is accompanied by a decreased SSS in the Arctic Ocean due to the additional freshwater input. The seasonal mean SIC anomalies show a similar picture: in DJF and MAM, the anomalies exhibit a pattern similar to the March anomaly, and JJA and SON to September. The SIC in the Central Arctic Ocean is largely unchanged, except for JJA, when it decreases. The comparison of the calendar-corrected and the uncorrected SIC anomalies revealed that, without calendar correction, the SIC is overestimated in SON and DJF, and in the Central Arctic also in MAM, for the LIG. In JJA and outside of the Central Arctic in MAM, it is underestimated. The largest deviations occur in SON, and exceed $-15\,\%$.

In addition to the SIC, the temporal evolution of the September sea ice area in the Arctic over 200 model years was investigated. For this purpose, the data from the simulations conducted for this thesis were complemented by the last 160 simulation years of a previous model run. In this way, multi-decadal variability could be visualised. Both the LIG and the PI simulation exhibit multi-decadal variability and, at first glance, it is not significantly more pronounced for one of the periods compared to the other. During the LIG, Arctic September sea ice area fluctuates roughly between $8 \times 10^6\,\mathrm{km}^2$ and just above $9 \times 10^6\,\mathrm{km}^2$. This is higher than observed in any of the PMIP4 models. The multi-model mean of maximum Arctic sea ice area in September was reported as $3.1 \times 10^6\,\mathrm{km}^2$, and the range as $0.22 \times 10^6\,\mathrm{km}^2$ to $7.47 \times 10^6\,\mathrm{km}^2$ (Otto-Bliesner et al., 2021). The LIG–PI anomalies for the September sea ice area range approximately between $-2.7 \times 10^6\,\mathrm{km}^2$ and

$-1.3 \times 10^6\,\mathrm{km}^2$. Without calendar correction, the sea ice area during the LIG is overestimated, but only by a small margin.

North Atlantic climate. The closer look at the climate in the North Atlantic region and the Arctic region showed that many of the observed changes are linked. SAT and SST anomalies show very similar changes, for instance. However, the anomalies are larger in amplitude over land than over the oceans. As mentioned before, the reason for this is the greater heat capacity of water compared to air. Another difference between SAT and SST anomalies is that there are significant changes in SAT for the Arctic Ocean, but not in SST. This is due to Arctic sea ice which can act as an insulator, keeping the temperature in the Arctic Ocean largely unchanging. The SSS is decreased in the Arctic Ocean, particularly around the sea ice margins, where the decline in SIC in JJA and SON was also most notable. The melting of sea ice increases freshwater input, thus lowering salinity.

The paleo calendar effect is largest in SON, as seen before. It leads to significant deviations between the corrected and the uncorrected data. The magnitude of deviations between the SAT anomalies for the two different calendars is almost the same as the largest anomalies between LIG and PI, and they are most pronounced for the mid- and high latitudes. Hence, an analysis of North Atlantic and Arctic climate during the LIG necessitates a calendar correction of the model output.

6 Conclusions

In the scope of this thesis, two experiments were performed to simulate the climate during the LIG and the PI. The objective was an investigation of the climate during the LIG, and of the effect of a calendar correction on model output for different regions. The changes in orbital forcing between LIG and PI led to an increase of TOA insolation on the NH during summer. As a result, temperatures were higher over the NH mid- and high latitudes in JJA and SON, and Arctic sea ice was reduced.

The surface air temperature anomalies indicate a strong warming over land (except for the Sahel and Southwest Asia) in JJA and a cooling over land in DJF during the LIG, in agreement with the LIG–PI insolation anomalies. The strongest JJA warming occurs over North America and Eurasia and reaches more than 8 °C. The cooling over the Sahel, India and South Asia in JJA is most likely caused by the enhanced summer monsoons in these regions, leading to increased cloud cover and thus less insolation reaching the surface.

The differences between the calendar-corrected and the uncorrected SAT anomalies are largest during SON, and are most pronounced over the NH continents and the Arctic region. If no calendar correction is applied, the SAT over NH continents is significantly underestimated and even leads to a reversal of the sign of the anomalies. The biggest impact is observed over Eurasia, with 6 °C warming due to the calendar correction, indicating that the paleo calendar effect is almost as big as the deviations between LIG and PI.

The precipitation anomalies show enhanced summer monsoons on the NH, and attenuated summer monsoons on the SH. This is accompanied by a northward shift of the ITCZ in JJA and a southward shift in DJF. The paleo calendar effect on precipitation is also largest in SON, but it particularly affects the low latitudes. It leads to an underestimation of the increase in the strength of NH summer monsoons and of the decrease in precipitation on the SH.

Sea surface temperature anomalies between LIG and PI largely show great sim-

ilarity to the SAT anomalies, but are mostly less intense. In JJA and SON, when strong warming occurs over NH continents, there is also a significant rise in SST in the NH oceans. The Central Arctic Ocean, however, remains largely unchanged, most likely because it is insulated from the atmosphere by sea ice. A region where strong SST anomalies occur year-round is the North Atlantic, which displays a dipole pattern in both SST and SSS that suggests a weaker meridional heat transport. The paleo calendar effect on SST anomalies shows a very similar pattern to the one on SAT anomalies, but it reaches a maximum of 2.8 °C in the NH mid-latitudes, approximately half of the value for the SAT. However, this is still a significant difference, and therefore a calendar correction is also advisable when analysing SST during the LIG.

The anomalies in sea surface salinity in the tropics seem to be linked to the precipitation anomalies to a great extent. SSS is decreased in regions of increased precipitation and associated freshwater input, and increased where it is drier during the LIG. In the Arctic region, changes in salinity are presumably strongly linked to melting or formation of sea ice. Finally, along the west coast of Africa, a decreased SSS is observed, suggesting weakened upwelling. The paleo calendar effect is relatively minor for SSS, except in the Arctic Ocean and the previously mentioned upwelling region.

The Arctic sea ice concentration was found to be slightly higher in March during the LIG than the PI, and considerably lower in September. During JJA and SON, SIC decreases in and around the Arctic Ocean, most notably along the sea ice margins. In the Bering Sea, an increase in SIC relative to the PI is observed year-round. The paleo calendar effect during SON leads to an overestimation of SIC of about 15 %, while the largest LIG–PI anomalies exceed 70 %.

The time series of the Arctic sea ice area revealed multi-decadal variability. At first glance, the LIG and the PI exhibit similar variability. However, this could be further investigated in the future using more sophisticated methods, for instance a wavelet analysis. The paleo calendar effect on the sea ice area is rather small com-

pared to the LIG–PI anomalies. In view of the uncertainty regarding Arctic summer sea ice, it is debatable whether a correction is necessary for investigations of the sea ice area. The impact on SIC was larger, though, rendering a calendar correction also advisable when analysing sea ice.

In conclusion, this study revealed the importance of applying a calendar correction for investigations of the LIG climate. Because the spring equinox is fixed to 21 March in the simulations, and acts as the starting point for the calendar conversion, the paleo calendar effect is minor in MAM and most pronounced in SON. Fixing the spring equinox to a certain date is an arbitrary choice. If another point along the orbit was chosen to be fixed across simulations, the paleo calendar effect would reach its maximum in a different season.

Especially for atmospheric variables, e.g. SAT or precipitation, the paleo calendar effect has a large impact on the analysis of paleoclimate simulations, and is comparable in magnitude to the LIG–PI anomalies. But the effects on the surface ocean and on sea ice are also not negligible and warrant a conversion of the data to the angular calendar. The regions most affected by the choice of calendar are mostly those where the largest anomalies between LIG and PI occur, which are primarily the mid- and high latitudes on the NH. Solely for the precipitation, the low latitudes are affected the most.

Previous studies on the paleo calendar effect have mostly focused on atmospheric variables. This study showed that it can also have a significant impact on the surface ocean and sea ice. In the future, it could be of interest to examine the impact on further variables, e.g. cloud cover or surface winds.

More importantly however, future work could further investigate the extent of Arctic summer sea ice, which is highly debated at the moment. In this regard, it might be interesting to perform simulations with an interactive Greenland ice sheet, as this was most likely reduced in thickness during the LIG. Further, more proxy data could also help to constrain this problem.

Acknowledgements

I would like to express my gratitude to my supervisors, Prof. Dr. Gerrit Lohmann and PD Dr. Martin Werner, for giving me the opportunity to write my master's thesis at the Alfred Wegener Institute and for their feedback and support during this time.

I am also deeply grateful to Fernanda Matos for all the guidance, feedback and support I received from her on this journey.

Many thanks to the members of the Paleoclimate Dynamics group who welcomed me warmly and supported me.

Finally, I would like to thank my family and friends, especially my sister, for always being there for me and encouraging me.

References

Bakker, P., Stone, E. J., Charbit, S., Gröger, M., Krebs-Kanzow, U., Ritz, S. P., Varma, V., Khon, V., Lunt, D. J., Mikolajewicz, U., Prange, M., Renssen, H., Schneider, B., & Schulz, M. (2013). Last interglacial temperature evolution - a model inter-comparison. *Climate of the Past*, *9*(2), 605–619, https://doi.org/10.5194/cp-9-605-2013 https://cp.copernicus.org/articles/9/605/2013/.

Balsamo, G., Beljaars, A., Scipal, K., Viterbo, P., Hurk, B. v. d., Hirschi, M., & Betts, A. K. (2009). A Revised Hydrology for the ECMWF Model: Verification from Field Site to Terrestrial Water Storage and Impact in the Integrated Forecast System. *Journal of Hydrometeorology*, *10*(3), 623–643, https://doi.org/10.1175/2008JHM1068.1 https://journals.ametsoc.org/view/journals/hydr/10/3/2008jhm1068_1.xml.

Barbi, D., Wieters, N., Gierz, P., Andrés-Martínez, M., Ural, D., Chegini, F., Khosravi, S., & Cristini, L. (2021). ESM-Tools version 5.0: a modular infrastructure for stand-alone and coupled Earth system modelling (ESM). *Geoscientific Model Development*, *14*(6), 4051–4067, https://doi.org/10.5194/gmd-14-4051-2021 https://gmd.copernicus.org/articles/14/4051/2021/.

Bartlein, P. J. & Shafer, S. L. (2019). Paleo calendar-effect adjustments in time-slice and transient climate-model simulations (paleocaladjust v1.0): impact and strategies for data analysis. *Geoscientific Model Development*, *12*(9), 3889–3913, https://doi.org/10.5194/gmd-12-3889-2019 https://gmd.copernicus.org/articles/12/3889/2019/.

Berger, A. (1988). Milankovitch theory and climate. *Reviews of Geophysics*, *26*(4), 624–657, https://doi.org/https://doi.org/10.1029/RG026i004p00624 https://agupubs.onlinelibrary.wiley.com/doi/abs/10.1029/RG026i004p00624.

Berger, A. & Loutre, M.-F. (1991). Insolation values for the climate of the last 10 million years. *Quaternary Science Reviews*, *10*, 297–317, https://doi.org/10.1016/0277-3791(91)90033-Q.

Burke, K. D., Williams, J. W., Chandler, M. A., Haywood, A. M., Lunt, D. J., & Otto-Bliesner, B. L. (2018). Pliocene and Eocene provide best analogs for near-future climates. *Proceedings of the National Academy of Sciences*, *115*(52), 13288–13293, https://doi.org/10.1073/pnas.1809600115.

CAPE (2006). Last Interglacial Arctic warmth confirms polar amplification of climate change. *Quaternary Science Reviews*, *25*(13), 1383–1400, https://doi.org/10.1016/j.quascirev.2006.01.033.

Craig, A., Valcke, S., & Coquart, L. (2017). Development and performance of a new version of the OASIS coupler, OASIS3-MCT_3.0. *Geoscientific Model Development*, *10*(9), 3297–3308, https://doi.org/10.5194/gmd-10-3297-2017. Pub-

lisher: Copernicus GmbH https://gmd.copernicus.org/articles/10/3297/2017/.

Cronin, T. (2010). *Paleoclimates: Understanding Climate Change Past and Present*. Columbia University Press https://books.google.de/books?id=X49VC6B65DEC.

Curtis, H. D. (2014). Chapter 3 - orbital position as a function of time. In H. D. Curtis (Ed.), *Orbital Mechanics for Engineering Students (Third Edition)* (pp. 145–186). Boston: Butterworth-Heinemann, third edition edition https://www.sciencedirect.com/science/article/pii/B9780080977478000037.

Dahl-Jensen, D., et al. (2013). Eemian interglacial reconstructed from a Greenland folded ice core. *Nature*, *493*(7433), 489–494, https://doi.org/10.1038/nature11789.

Danilov, S., Wang, Q., Timmermann, R., Iakovlev, N., Sidorenko, D., Kimmritz, M., Jung, T., & Schröter, J. (2015). Finite-Element Sea Ice Model (FESIM), version 2. *Geoscientific Model Development*, *8*(6), 1747–1761, https://doi.org/10.5194/gmd-8-1747-2015. Publisher: Copernicus GmbH https://gmd.copernicus.org/articles/8/1747/2015/.

Danilov, S., Sidorenko, D., Wang, Q., & Jung, T. (2017). The finite-volume sea ice–ocean model (fesom2). *Geoscientific Model Development*, *10*(2), 765–789, https://doi.org/10.5194/gmd-10-765-2017 https://gmd.copernicus.org/articles/10/765/2017/.

Duboc, B., Meissner, K. J., Menviel, L., Yeung, N. K. H., Hoogakker, B., Ziehn, T., & Chamberlain, M. (2025). Simulated ocean oxygenation during the interglacials MIS 5e and MIS 9e. *Climate of the Past*, *21*(6), 1093–1122, https://doi.org/10.5194/cp-21-1093-2025.

Dutton, A., Carlson, A. E., Long, A. J., Milne, G. A., Clark, P. U., DeConto, R., Horton, B. P., Rahmstorf, S., & Raymo, M. E. (2015). Sea-level rise due to polar ice-sheet mass loss during past warm periods. *Science*, *349*(6244), aaa4019, https://doi.org/10.1126/science.aaa4019 https://www.science.org/doi/abs/10.1126/science.aaa4019.

ECMWF (2017a). *IFS Documentation CY43R3 - Part III: Dynamics and numerical procedures*. Number 3. ECMWF https://www.ecmwf.int/node/17735.

ECMWF (2017b). *IFS Documentation CY43R3 - Part IV: Physical processes*. Number 4. ECMWF https://www.ecmwf.int/node/17736.

ECMWF (2017c). *IFS Documentation CY43R3 - Part VII: ECMWF wave model*. Number 7. ECMWF https://www.ecmwf.int/node/17739.

Epstein, E. S. (1991). On obtaining daily climatological values from monthly means. *J. Clim.*, *4*(3), 365–368.

Eyring, V., Bony, S., Meehl, G., Senior, C., Stevens, B., Ronald, S., & Taylor, K. (2016). Overview of the coupled model intercomparison project phase 6 (cmip6) experimental design and organization. *Geoscientific Model Development*, *9*, 1937–1958, https://doi.org/10.5194/gmd-9-1937-2016.

Grotzinger, J. & Jordan, T. (2017). *System Klima*, (pp. 401–428). Springer Berlin Heidelberg: Berlin, Heidelberg https://doi.org/10.1007/978-3-662-48342-8_15.

Hays, J. D., Imbrie, J., & Shackleton, N. J. (1976). Variations in the earth's orbit: Pacemaker of the ice ages: For 500, 000 years, major climatic changes have followed variations in obliquity and precession. *Science*, *194*(4270), 1121–1132, https://doi.org/10.1126/science.194.4270.1121 http://dx.doi.org/10.1126/science.194.4270.1121.

Imbrie, J., Berger, A., Boyle, E. A., Clemens, S. C., Duffy, A., Howard, W. R., Kukla, G., Kutzbach, J., Martinson, D. G., McIntyre, A., Mix, A. C., Molfino, B., Morley, J. J., Peterson, L. C., Pisias, N. G., Prell, W. L., Raymo, M. E., Shackleton, N. J., & Toggweiler, J. R. (1993). On the structure and origin of major glaciation cycles 2. The 100,000-year cycle. *Paleoceanography*, *8*(6), 699–735, https://doi.org/10.1029/93PA02751 https://onlinelibrary.wiley.com/doi/abs/10.1029/93PA02751.

IPCC (2021). *Climate Change 2021: The Physical Science Basis. Contribution of Working Group I to the Sixth Assessment Report of the Intergovernmental Panel on Climate Change*, volume In Press. Cambridge, United Kingdom and New York, NY, USA: Cambridge University Press.

Joussaume, S. & Braconnot, P. (1997). Sensitivity of paleoclimate simulation results to season definitions. *Journal of Geophysical Research: Atmospheres*, *102*(D2), 1943–1956, https://doi.org/https://doi.org/10.1029/96JD01989 https://agupubs.onlinelibrary.wiley.com/doi/abs/10.1029/96JD01989.

Kageyama, M., Braconnot, P., Chiessi, C. M., Rehfeld, K., Ait Brahim, Y., Dütsch, M., Gwinneth, B., Hou, A., Loutre, M.-F., Hendrizan, M., Meissner, K., Mongwe, P., Otto-Bliesner, B., Pezzi, L. P., Rovere, A., Seltzer, A., Sime, L., & Zhu, J. (2024). Lessons from paleoclimates for recent and future climate change: opportunities and insights. *Frontiers in Climate*, *6*, https://doi.org/10.3389/fclim.2024.1511997. Publisher: Frontiers https://www.frontiersin.org/journals/climate/articles/10.3389/fclim.2024.1511997/full.

Komen, G. J., Cavaleri, L., Donelan, M., Hasselmann, K., Hasselmann, S., & Janssen, P. A. E. M. (1994). *Dynamics and Modelling of Ocean Waves*. Cambridge University Press.

Kremer, A., Stein, R., Fahl, K., Ji, Z., Yang, Z., Wiers, S., Matthiessen, J., Forwick, M., Löwemark, L., O'Regan, M., Chen, J., & Snowball, I. (2018). Changes in sea ice cover and ice sheet extent at the Yermak Plateau during the last 160 ka – Reconstructions from biomarker records. *Quaternary Science Reviews*, *182*, 93–108, https://doi.org/10.1016/j.quascirev.2017.12.016.

Kukla, G. J., et al. (2002). Last interglacial climates. *Quaternary Research*, *58*(1), 2–13, https://doi.org/https://doi.org/10.1006/qres.2001.2316 https://www.sciencedirect.com/science/article/pii/S0033589401923166.

Kutzbach, J. E. (1981). Monsoon climate of the early holocene: Climate experiment with the earth's orbital parameters for 9000 years ago. *Science*, *214*(4516), 59–61, https://doi.org/10.1126/science.214.4516.59 https://www.science.org/doi/abs/10.1126/science.214.4516.59.

Kutzbach, J. E. & Gallimore, R. G. (1988). Sensitivity of a coupled atmosphere/mixed layer ocean model to changes in orbital forcing at 9000 years b.p. *Journal of Geophysical Research: Atmospheres*, *93*(D1), 803–821, https://doi.org/https://doi.org/10.1029/JD093iD01p00803 https://agupubs.onlinelibrary.wiley.com/doi/abs/10.1029/JD093iD01p00803.

Large, W. G. & Yeager, S. G. (2009). The global climatology of an interannually varying air–sea flux data set. *Climate Dynamics*, *33*(2), 341–364, https://doi.org/10.1007/s00382-008-0441-3.

Laskar, J., Joutel, F., & Boudin, F. (1993). Orbital, precessional, and insolation quantities for the earth from -20 myr to +10 myr. *Astronomy and Astrophysics*, *270*, 522–533.

Laskar, J., Robutel, P., Joutel, F., Gastineau, M., Correia, A. C. M., & Levrard, B. (2004). A long-term numerical solution for the insolation quantities of the earth. *Astronomy and Astrophysics*, *428*(1), 261–285, https://doi.org/10.1051/0004-6361:20041335 http://dx.doi.org/10.1051/0004-6361:20041335.

Milanković, M. (1941). *Kanon der Erdbestrahlung und seine Anwendung auf das Eiszeitproblem*. Posebna izdanja. Königlich Serbische Akademie https://books.google.de/books?id=JbfZjgEACAAJ.

Otto-Bliesner, B. L., Rosenbloom, N., Stone, E. J., McKay, N. P., Lunt, D. J., Brady, E. C., & Overpeck, J. T. (2013). How warm was the last interglacial? New model–data comparisons. *Philosophical Transactions of the Royal Society A: Mathematical, Physical and Engineering Sciences*, *371*(2001), 20130097, https://doi.org/10.1098/rsta.2013.0097. Publisher: Royal Society https://royalsocietypublishing.org/doi/10.1098/rsta.2013.0097.

Otto-Bliesner, B. L., et al. (2017). The pmip4 contribution to cmip6 - part 2: Two interglacials, scientific objective and experimental design for holocene and last interglacial simulations. *Geoscientific Model Development*, *10*(11), 3979–4003, https://doi.org/10.5194/gmd-10-3979-2017 https://gmd.copernicus.org/articles/10/3979/2017/.

Otto-Bliesner, B. L., et al. (2021). Large-scale features of Last Interglacial climate: results from evaluating the *lig127k* simulations for the Coupled Model Intercomparison Project (CMIP6)–Paleoclimate Modeling Intercomparison Project (PMIP4). *Climate of the Past*, *17*(1), 63–94, https://doi.org/10.5194/cp-17-63-2021 https://cp.copernicus.org/articles/17/63/2021/.

Pollard, D. & Reusch, D. B. (2002). A calendar conversion method for monthly mean paleoclimate model output with orbital forcing. *Journal of Geophysical Research: Atmospheres*, *107*(D22), ACL 3–1–ACL 3–7, https://doi.org/https://doi.org/10.1029/2002JD002126 https://agupubs.onlinelibrary.wiley.com/doi/abs/10.1029/2002JD002126.

Raymo, M. E. & Huybers, P. (2008). Unlocking the mysteries of the ice ages. *Nature*, *451*(7176), 284–285, https://doi.org/10.1038/nature06589 http://dx.doi.org/10.1038/nature06589.

Rohling, E. J., Marino, G., & Grant, K. M. (2015). Mediterranean climate and oceanography, and the periodic development of anoxic events (sapropels). *Earth-Science Reviews*, *143*, 62–97, https://doi.org/10.1016/j.earscirev.2015.01.008.

Ruddiman, W. F. (2014). *Earth's Climate*. W. H. Freeman and Company, third edition.

Scholz, P., Sidorenko, D., Gurses, O., Danilov, S., Koldunov, N., Wang, Q., Sein, D., Smolentseva, M., Rakowsky, N., & Jung, T. (2019). Assessment of the Finite-volumE Sea ice-Ocean Model (FESOM2.0) – Part 1: Description of selected key model elements and comparison to its predecessor version. *Geoscientific Model Development*, *12*(11), 4875–4899, https://doi.org/10.5194/gmd-12-4875-2019.

Scholz, P., Sidorenko, D., Danilov, S., Wang, Q., Koldunov, N., Sein, D., & Jung, T. (2022). Assessment of the Finite-VolumE Sea ice–Ocean Model (FESOM2.0) – Part 2: Partial bottom cells, embedded sea ice and vertical mixing library CVMix. *Geoscientific Model Development*, *15*(2), 335–363, https://doi.org/10.5194/gmd-15-335-2022.

Schulzweida, U. (2023). Cdo user guide https://doi.org/10.5281/zenodo.10020800.

Scussolini, P., Bakker, P., Guo, C., Stepanek, C., Zhang, Q., Braconnot, P., Cao, J., Guarino, M.-V., Coumou, D., Prange, M., Ward, P. J., Renssen, H., Kageyama, M., Otto-Bliesner, B., & Aerts, J. C. J. H. (2019). Agreement between reconstructed and modeled boreal precipitation of the Last Interglacial. *Science Advances*, *5*(11), eaax7047, https://doi.org/10.1126/sciadv.aax7047.

Shi, X., Werner, M., Krug, C., Brierley, C. M., Zhao, A., Igbinosa, E., Braconnot, P., Brady, E., Cao, J., D'Agostino, R., Jungclaus, J., Liu, X., Otto-Bliesner, B., Sidorenko, D., Tomas, R., Volodin, E. M., Yang, H., Zhang, Q., Zheng, W., & Lohmann, G. (2022). Calendar effects on surface air temperature and precipitation based on model-ensemble equilibrium and transient simulations from PMIP4 and PACMEDY. *Climate of the Past*, *18*(5), 1047–1070, https://doi.org/10.5194/cp-18-1047-2022 https://cp.copernicus.org/articles/18/1047/2022/.

Sicard, M., Coxall, H. K., Koenigk, T., Karami, M. P., Jakobsson, M., & O'Regan, M. (2023). Similarities and Differences in Arctic Sea-Ice Loss During the Solar-Forced Last Interglacial Warming (127 Kyr BP) and CO2-Forced Future Warming.

50(24), e2023GL104782, https://doi.org/10.1029/2023GL104782 https://onlinelibrary.wiley.com/doi/abs/10.1029/2023GL104782.

Sime, L. C., Sivankutty, R., Vallet-Malmierca, I., de Boer, A. M., & Sicard, M. (2023). Summer surface air temperature proxies point to near-sea-ice-free conditions in the arctic at 127 ka. *Climate of the Past*, *19*(4), 883–900, https://doi.org/10.5194/cp-19-883-2023 https://cp.copernicus.org/articles/19/883/2023/.

Stein, R., Fahl, K., Gierz, P., Niessen, F., & Lohmann, G. (2017). Arctic Ocean sea ice cover during the penultimate glacial and the last interglacial. *Nature Communications*, *8*(1), 373, https://doi.org/10.1038/s41467-017-00552-1.

Streffing, J., et al. (2022). AWI-CM3 coupled climate model: description and evaluation experiments for a prototype post-CMIP6 model. *Geoscientific Model Development*, *15*(16), 6399–6427, https://doi.org/10.5194/gmd-15-6399-2022 https://gmd.copernicus.org/articles/15/6399/2022/.

Turney, C. S. & Jones, R. T. (2010). Does the Agulhas Current amplify global temperatures during super-interglacials? *Journal of Quaternary Science*, *25*(6), 839–843, https://doi.org/10.1002/jqs.1423. _eprint: https://onlinelibrary.wiley.com/doi/pdf/10.1002/jqs.1423 https://onlinelibrary.wiley.com/doi/abs/10.1002/jqs.1423.

Vermassen, F., O'Regan, M., de Boer, A., Schenk, F., Razmjooei, M., West, G., Cronin, T. M., Jakobsson, M., & Coxall, H. K. (2023). A seasonally ice-free Arctic Ocean during the Last Interglacial. *Nature Geoscience*, *16*(8), 723–729, https://doi.org/10.1038/s41561-023-01227-x.

Yin, Q. & Berger, A. (2015). Interglacial analogues of the holocene and its natural near future. *Quaternary Science Reviews*, *120*, 28–46, https://doi.org/https://doi.org/10.1016/j.quascirev.2015.04.008 https://www.sciencedirect.com/science/article/pii/S027737911500150X.

A Appendix

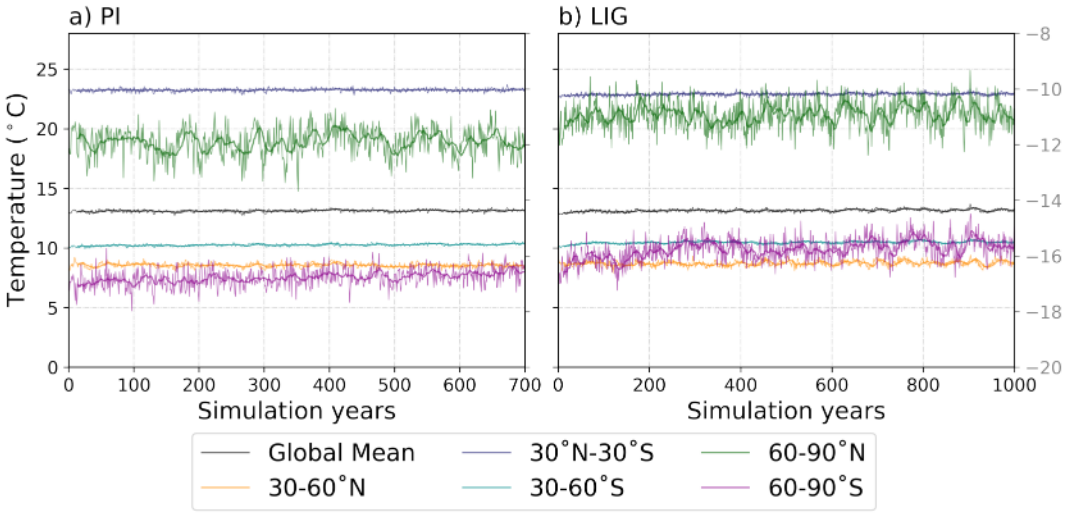

Figure A.1: Surface air temperature per region for the simulations that the ones featured here were branched off from. The SAT shows no significant trends, suggesting that the simulations are in quasi-equilibrium. This figure was kindly provided by Fernanda Matos.

Declaration of Authorship and Consent for Checking With Plagiarism Software and the Declaration of Publication for Bachelor's and Master's Thesis

A – Declaration of authorship

I hereby affirm that I have written the present work independently and have used no sources or aids other than those indicated. All parts of my work that have been taken from other works, either verbatim or in terms of meaning, have been marked as such, indicating the source. The same applies to drawings, sketches, pictorial representations and sources from the Internet, including AI-based applications or tools. The work has not yet been submitted in the same or a similar form as a final examination paper.

B – Declaration regarding the publication of bachelor's and master's thesis

Two years after graduation, the thesis is offered to the archive of the University of Bremen for permanent archiving. The following are archived:

1) Master's theses with a local or regional focus, as well as per subject and academic year 10% of all Master's theses.

2) Bachelor's thesis for the first and last bachelor's degrees per subject and year.

☒ I agree that my thesis may be viewed by third parties in the university archive for academic purposes.

☒ I agree that my thesis may be viewed by third parties for academic purposes in the university archive after 30 years (in accordance with §7 para. 2 BremArchivG).

☐ I do **not** consent to my thesis being made available in the university archive for third parties to view for academic purposes.

C – Declaration of consent for electronic checking of the work for plagiarism

Submitted papers can be checked for plagiarism using qualified software in accordance with § 18 of the General Section of the Bachelor's or Master's Degree Examination Regulations of the University of Bremen. For the purpose of checking for plagiarism, the upload to the server is done using the plagiarism software currently used by the University of Bremen.

☒ I agree that the work I have submitted and written will be stored permanently on the external server of the plagiarism software currently used by the University of Bremen, in a library belonging to the institution (accessed only by the University of Bremen), for the above-mentioned purpose.

☐ I do **not** consent to the work I submitted and wrote being permanently stored on the external server of the plagiarism software currently used by the University of Bremen, in a library belonging to the institution (accessed only by the University of Bremen), for the above-mentioned purpose.

Consent to the permanent storage of the text is voluntary. Consent can be withdrawn at any time by making a declaration to this effect to the University of Bremen, with effect for the future. Further information on the checking of written work using plagiarism software can be found in the data protection and usage concept. This can be found on the University of Bremen website.

With my signature, I confirm that I have read and understood the above explanations and confirm the accuracy of the information provided.

Bremen, 29 August 2025 Mareike Mammes